Fluctuations at a constrained liquid-solid interface

Abhishek Chaudhuri
Raman Research Institute, C. V. Raman Avenue, Sadashivanagar, Bangalore - 560080, India[*]

Debasish Chaudhuri
Max Planck Institute for the Physics of Complex Systems, Nöthnitzer Strasse 38, 01187 Dresden, Germany[†]

Surajit Sengupta
S. N. Bose National Center for Basic Sciences, JD Block, Sector 3, Salt Lake, Kolkata - 700098, India[‡]

(Received 19 March 2007; published 21 August 2007)

We study the interface between a solid trapped within a bath of liquid by a suitably shaped nonuniform external potential. Such a potential may be constructed using lasers, external electric or magnetic fields, or a surface template. We study a two-dimensional case where a thin strip of solid, created in this way, is surrounded on either side by a bath of liquid with which it can easily exchange particles. Since height fluctuations of the interface cost energy, this interface is constrained to remain flat at all length scales. However, when such a solid is stressed by altering the depth of the potential beyond a certain limit, it responds by relieving stress by novel interfacial fluctuations, which involve addition or deletion of entire lattice layers of the crystal. This "layering" transition is a generic feature of the system regardless of the details of the interaction potential. We show how such interfacial fluctuations influence mass, momentum, and energy transport across the interface. Tiny momentum impulses produce weak shock waves, which travel through the interface and cause the spallation of crystal layers into the liquid. Kinetic and energetic constraints prevent spallation of partial layers from the crystal, a fact which may be of some practical use. We also study heat transport through the liquid-solid interface and obtain the resistances in liquid, solid, and interfacial regions (Kapitza resistance) as the solid undergoes such layering transitions. Heat conduction, which shows strong signatures of the structural transformations, can be understood using a free volume calculation.

DOI: 10.1103/PhysRevE.76.021603 PACS number(s): 68.08.−p, 68.65.−k, 62.50.+p, 44.15.+a

I. INTRODUCTION

Interfaces between coexisting phases in condensed matter systems possesses an intrinsic width determined by competition between bulk and surface energies [1–4], which is usually further broadened by capillary fluctuations [5,6], viz., random fluctuations of the interface away from its mean position. The latter is a direct manifestation of the fact that translations of the interface in a direction perpendicular to its plane cost no energy [7]. Such capillary fluctuations actually cause the interfacial width to diverge [7,8] with a cutoff determined by the system size. External potentials, e.g., gravitational fields or coupling to a substrate however [9–11], tend to round off this divergence and set additional length scales, absent in the free system. If one or both of the phases happens to be a solid, then long-ranged elastic energy costs for deforming the interface may also limit the broadening of the interface in equilibrium [12]. Nevertheless, the analog of capillary fluctuations, viz., crystallization waves have been experimentally observed at liquid-solid interfaces [13]. It is, of course, also possible to suppress interfacial capillary fluctuations by position-dependent chemical potentials, which break the translational symmetry of the interface explicitly [14]. One would expect that such interfaces would remain essentially flat over all length scales and therefore be completely inert.

We show, in this paper, that this is not so. Surprisingly, there are novel fluctuations and phenomena associated with such constrained interfaces, which have static as well as dynamic consequences. Particles are transferred across the interface in new and interesting ways. A liquid-solid interface constructed in such a fashion can have physically interesting height fluctuations while at the same time remaining flat. The system manages this by selecting only those fluctuations which involve changes in height by a single atomic spacing and have a wavelength equal to the size of system in the transverse direction. Further, such interfacial fluctuations are driven by the elastic response of the solid to stresses imposed by the external potential. As the depth of the trapping potential is gradually increased, the solid accommodates this stress by incorporating layers of atoms from the liquid, either only parallel to the interface or alternately perpendicular and parallel in a cyclical fashion, depending on the nature of the interactions. We believe that some of our predictions may be directly checked for liquid-solid interfaces in atomic, as well as colloidal systems where the chemical potential field may be provided either by a laser trap or by a patterned substrate. Needless to say, such fluctuations are expected to be observed only in systems where the overall size is small—of the order of only a few atomic spacings in the transverse direction. Preliminary results of our studies of this system have been published in Refs. [15,16].

This paper is organized as follows. We begin, in the next section, by showing how a two-dimensional liquid-solid in-

[*]abhishek@rri.res.in
[†]debc@pks.mpg.de
[‡]surajit@bose.res.in

terface may be produced using a nonuniform external potential. Monte Carlo (MC) computer simulations [17] in the constant number, area, and temperature (*NAT*) ensemble are set up to realize this explicitly for particles interacting with hard disk, soft disk, and Lennard-Jones potentials. The interface is then characterized using a variety of thermodynamic and structural quantities, which are measured as a function of the perpendicular distance from the interface. As a function of the depth of the potential well, the trapped solid undergoes what we have called "layering" transitions [15,16,18–21], which involve the addition (or removal) of an entire layer of a solid from (or into) the surrounding liquid through the interface. This transition is described in detail for the hard disk system in Sec. III. The layering transition is accompanied by a sharp jump in the density of the solid. We obtain this density jump within a mean field, thermodynamic approach [20]. A comparison of the predictions of the thermodynamic theory and our MC computer experiments show the theory to be approximately correct to within a few percent. We show that the layering transition is a novel mechanism by which a stressed nano solid constrained by an external potential can respond plastically to large stresses *without* nucleating dislocations or cracks [22,23]. We establish that this phenomenon is general and is independent of the particular interatomic potential used. In Sec. IV, we describe the kinetics of the layering transition. In Sec. V we explore how mass and momentum are transported across the liquid-solid interface and especially the role of the layering transition on the transport coefficients. Molecular dynamics (MD) simulations in the constant number, area, and energy (*NAE*) ensemble [17] are carried out for this purpose. We show in this paper that (1) fluctuations associated with these transitions are of a special kind always involving the transfer of complete layers of solid; (2) these fluctuations offer resistance to the transfer of momentum and energy through the interface; and (3) the resistance is maximum when the energy matches that required to raise a complete lattice layer from within the potential well into the surrounding liquid. We study the stability of surface kinks at the liquid-solid interface in the hard disk system. We then study the response of the interface to weak acoustic shocks [24], which are shown to cause *spallation* of complete lattice layers if the incident energy of the shock is large enough. In Sec. VI we use nonequilibrium molecular dynamics to study heat transport [21] through the liquid-solid interface in soft disks and obtain the conductance of the system in different regions, heat current and contact, or Kapitza resistance [25,26] of the interface as a function of the depth of the potential well. The heat conduction is particularly sensitive to the fluctuations in the direction of current flow. We present an approximate free-volume-type calculation that qualitatively captures the response of the heat conductance to the internal changes in the solid induced by the trapping potential [21]. Finally, in Sec. VII we conclude after discussing some consequences of our study and its relevance to experiments.

II. CONSTRAINED LIQUID-SOLID INTERFACE: STATIC PROPERTIES

In this section, we explore the possibility of creating a patterned sequence of confined solid and liquid regions using

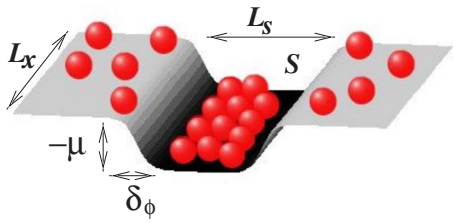

FIG. 1. (Color online) A schematic diagram of the system showing the liquid and solid regions produced by the external chemical potential of depth $-\mu$. The various dimensions mentioned in the text are also marked in the figure [15,16].

an external, space-dependent, chemical potential field $\phi(\mathbf{r})$. Consider a two-dimensional system (see Fig. 1) of N atoms of average density (packing fraction) $\eta=\pi N/4A$ within a rectangular cell of size $A=L_xL_y$, where the central region $\mathcal{S}$ of area $A_s=L_xL_s$ is occupied by N_s atoms arranged as a crystalline solid of density $\eta_s>\eta$, while the rest of the cell is filled with liquid of density $\eta_\ell<\eta$. The difference in density is produced by an external field $\phi(\mathbf{r})=-\mu$ for $\mathbf{r}\in\mathcal{S}$, increasing sharply but smoothly to zero elsewhere with a hyperbolic tangent profile of width δ_ϕ. How may $\phi(\mathbf{r})$ be realized in practice? In model solids like colloids [27], one may use a surface template to create a static pattern [28]. In real systems, as well as colloids [29], one may be able to use laser traps [30] or nonuniform electric or magnetic fields. Usual laser traps for alkali metals or rare gas atoms are in the range of 10 mK for which a power of about 100 mW is required [31]. For colloidal systems, required laser powers are even lower [32].

We first describe our results for a system where the atoms interact with a *hard disk* potential [33], which is infinitely repulsive if the distance r_{ij} between two atoms i and j is less than σ, the hard disk diameter, and zero otherwise. We show later that the results for more realistic potentials [17], e.g., soft disk or Lennard-Jones are qualitatively similar. We have chosen $\delta_\phi=\sigma/4$, where σ is the hard disk diameter and sets the scale of length. The energy scale for this system is set by k_BT, where k_B is the Boltzmann constant and T is the temperature. In our simulations we set $\sigma=1$ and $k_BT=1$ unless otherwise stated.

The full configuration-dependent Hamiltonian is $\mathcal{H}=\Sigma_{ij}u(\mathbf{r}_{ij})+\Sigma_i\phi(\mathbf{r}_i)$. We have carried out extensive MC simulations with usual Metropolis moves [17], periodic boundary conditions in both directions, and in the constant number, area, and temperature ensemble to obtain the equilibrium behavior of this system for different μ at a fixed average η. $N=1200$ particles occupy an area $A=22.78\times59.18$ with the solid occupying the central third of the cell of size $L_s=19.73$. The initial configuration is chosen to be a liquid with $\eta=0.699$, close to but slightly lower than the bulk freezing density $\eta_f=0.706$ [33]. On equilibration, $\mathcal{S}$ contains a solid with the close-packed planes parallel to the solid-liquid interfaces, which lie, at all times, along the lines where $\phi(y)\to0$. The equilibration time is large and many ($\sim10^7$) Monte Carlo steps (MCS) are discarded before results shown in Figs. 2–7 are obtained.

The density $\eta(y)$, coarse grained over strips of width $\sim\sigma$, varies from its value η_ℓ in the liquid to η_s as we move into

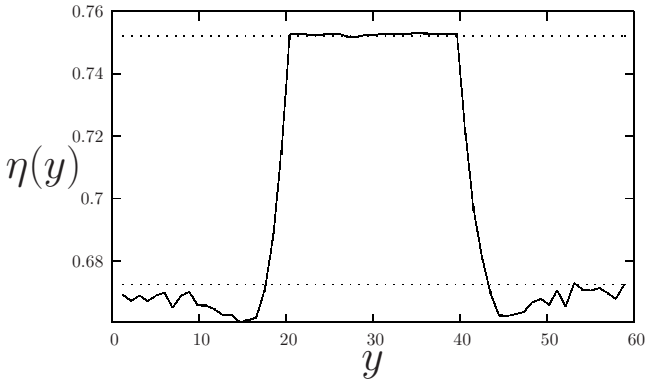

FIG. 2. The density profile $\eta(y)$ coarse grained over strips of width σ (averages taken over 10^3 MC configurations each separated by 10^3 MCS) at $\mu=6$. The dotted lines show the predictions for liquid density $\eta_\ell=0.6725$ and solid density $\eta_s=0.752$ from a simple thermodynamic theory presented in Sec. III A [15].

the region $\mathcal{S}$ (Fig. 2). Averages are taken over 10^3 MC configurations each separated by 10^3 MC steps. The trap depth $\mu=6$, supports an equilibrium solid of density $\eta_s=0.753$ in contact with a fluid of density $\eta_\ell=0.672$. The horizontal lines are predictions of a simple free-volume-based theory ([15]) for η_s and η_ℓ. We discuss the theory in Sec. III A. A superposition of atomic positions shows a static, flat, liquid-solid interface with the solidlike order gradually vanishing into the liquid (Fig. 3). We have thus created a thin nanosized crystal, which is 21 atomic layers wide (for a trap depth, $\mu=6$) and is flanked on either side by liquid separated by two liquid-solid interfaces.

The bond orientational order parameter $\langle\psi_6(y)\rangle$ where the local value of ψ_6 for a particle i located at $\mathbf{r}_i=(x,y)$ is given by

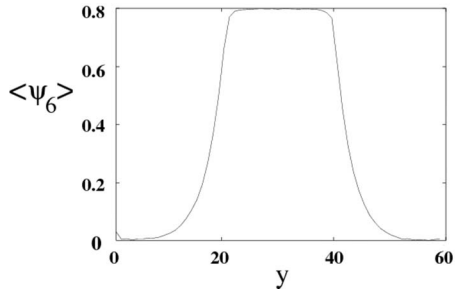

FIG. 4. Bond orientational order parameter across the liquid-solid interface for a 21-layered solid at $\mu=6$ surrounded by liquid on both sides.

$$\psi_{6,i}=\frac{1}{N_i}\sum_j \exp(6i\theta_{ij}). \tag{1}$$

The sum is over the $j\in N_i$ neighbors of ith particle, and θ_{ij} is the angle between the vector $\mathbf{r}_{ij}$ and an arbitrary but fixed reference axis. To obtain $\langle\psi_6(y)\rangle$, this quantity is coarse grained over strips of width σ (averages taken over 10^3 MC configurations each separated by 10^3 MCS). This shows a sharp rise from zero to a value close to one, as we move into the region $\mathcal{S}$ (Fig. 4). This indicates that the particles in $\mathcal{S}$ maintain hexatic order. However, this does not necessarily justify the phase to be a solid. Therefore, there is the need to calculate the solid order parameter.

The order parameters corresponding to the solid phase are the Fourier components of the (nonuniform) density-density correlation $\langle\rho(\mathbf{r}_i)\rho(\mathbf{r}_j)\rangle$ calculated at the reciprocal lattice points $\{\mathbf{G}\}$. This (infinite) set of numbers are all zero (for $\mathbf{G}\neq 0$) in a uniform liquid phase and nonzero in a solid. We restrict ourselves to the star consisting of the six smallest reciprocal lattice vectors of the two-dimensional triangular

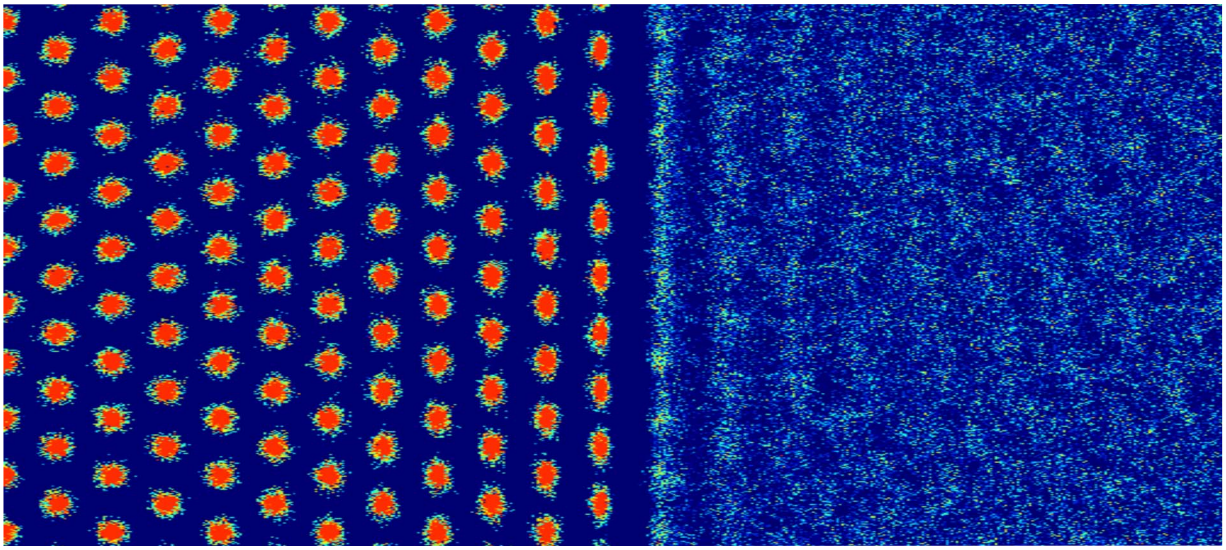

FIG. 3. (Color online) Solid-liquid interface at $\mu=8$. Superposition of 500 configurations separated by 10^3 MCS showing a solidlike order (red: high η) gradually vanishing into the fluid (blue: low η) across a well defined solid-fluid interface.

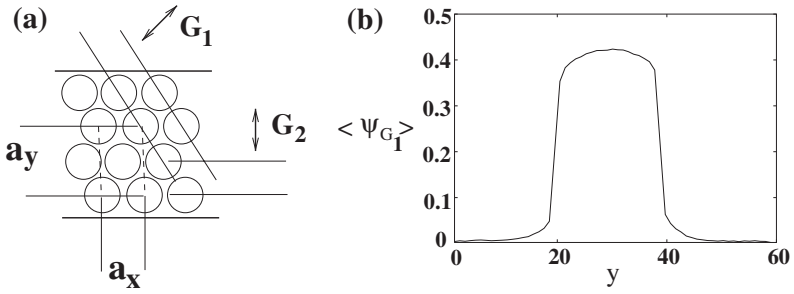

FIG. 5. (a) The reciprocal lattice vectors $\mathbf{G}_1$ and $\mathbf{G}_2$, and the rectangular unit cell. (b) Solid order parameter corresponding to $\mathbf{G}_1$ is nonzero in the region $\mathcal{S}$ at $\mu=6$, indicating a solid.

lattice. In modulated liquid phase, the Fourier components corresponding to two out of these six vectors, e.g., those in the direction perpendicular to the interface $\mathbf{G}_2$ are nonzero. The other four components of this set, which are equivalent by symmetry ($\mathbf{G}_1$), are zero in the (modulated) liquid and nonzero in the solid (if there is true long-ranged order). Thus, we use the following order parameter:

$$\langle \psi_{\mathbf{G}_k} \rangle = \frac{1}{N^2} \left\langle \left| \sum_{i,j=1}^{N} \exp(-i\mathbf{G}_k \cdot \mathbf{r}_{ij}) \right| \right\rangle, \tag{2}$$

where $\mathbf{r}_{ij}=\mathbf{r}_i-\mathbf{r}_j$. The solid order parameter so defined, in the direction $\mathbf{G}_1$ (see Fig. 5) and the others equivalent to it by symmetry is nonzero in the region $\mathcal{S}$, indicating the nucleation of a solid phase. Note that $\langle \psi_6 \rangle$ shows a larger interfacial region than that obtained from $\langle \psi_{\mathbf{G}_1} \rangle$. This is because the liquid near the liquid-solid interface is orientationally highly ordered due to the proximity of the solid.

The structure factor describes density correlations in Fourier space,

$$S(k) = N^{-1} \langle \rho(k) \rho(-k) \rangle, \tag{3}$$

where $\rho(k)=\Sigma_{i=1}^{N} \exp(i\mathbf{k}\cdot\mathbf{r}_i)$. In a simulation with periodic boundaries, $\mathbf{k}$ is restricted by the periodicity of the system, i.e., with the simulation box. The two-dimensional structure factor shows sharp peaks at triangular lattice positions for the solid region and isotropic ring pattern for the liquid (Fig. 6). The interfacial region also shows diffuse peaks at approximately triangular lattice positions indicating once more that the interfacial region has considerable orientational and short-ranged translational order.

Before we end this section, we must voice a note of caution about the identity of phases in small and confined systems similar to the one we have here. It is well known, for example, that in two dimensions it is impossible to obtain a solid with true long-ranged order [34]. Displacement correlations defined as $\langle \mathbf{u}(r) \cdot \mathbf{u}(0) \rangle$, where the displacement vector $\mathbf{u}$ is measured with respect to the zero temperature perfectly crystalline reference solid, grow as $\ln(r)$. This implies that true Bragg peaks are impossible in two dimensions. Nevertheless, finite size and lack of complete averaging can lead to structure factors with sharp peaks, while obtaining the true logarithmic divergence may need a considerable amount of computational effort. For a solid confined to a two-dimensional channel, the situation is even more dramatic. The displacement correlations now increase linearly with system size [35] for distances larger than a crossover length $\sim L_s \ln(L_s)$. The structure factor should show true Bragg peaks for reflections from planes parallel to the confining walls and should be diffuse in the other directions, implying therefore *smectic*-like ordering throughout. In this paper, however, we continue to use the words "solid" and "liquid" in the usual sense referring to the presence or lack of solid-like order as shown in Figs. 3 and 5. This is mainly due to the fact that our motivation of this study is to probe and understand the properties of small (nano) systems. For such systems with channel length L_x not much larger than L_s the phonon fluctuations are suppressed and cannot destabilize the solid. However, even for very large strips where phonon fluctuation destabilizes a solid to a smectic phase, layering transitions are expected to occur [36] and some associated properties such as acoustic spallation of layers and large change in heat conduction, which we describe in this paper, are expected to remain operative. We must, at the same time, keep in mind that some of the properties of the confined solid, including the layering transition and the ease of spallation of solid layers in response to weak acoustic shock (to be discussed below), may in fact, be a consequence of incomplete ordering.

III. LAYERING TRANSITION

We now calculate the difference in densities between the solid and liquid regions $\Delta\eta=(\eta_s-\eta_\ell)$ as a function of the

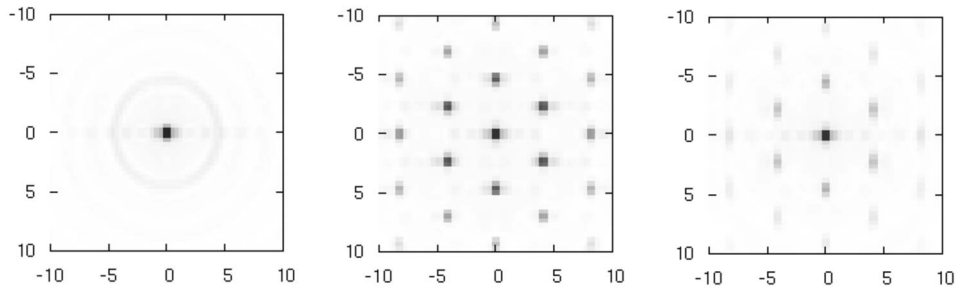

FIG. 6. From left to right, the three view graphs show structure factors for the liquid, the solid, and the interfacial regions, respectively, at $\mu=6$.

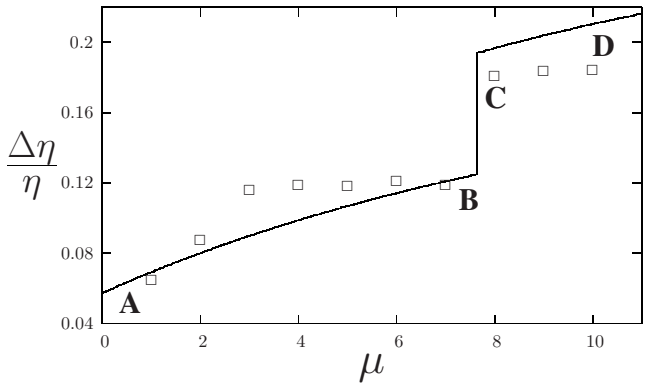

FIG. 7. Plot of the equilibrium fractional density change $\Delta\eta/\eta$ as a function of μ [points (MC data), solid line (free volume theory)], showing discontinuous jump at $\mu \approx 8$. The labels A–D mark the stable 21 layer solid (A), the transition (B and C) and the stable 22 layer solid (D), respectively.

strength of the external field μ. While $\Delta\eta/\eta$ increases with increasing μ as expected, the smooth increase is punctuated by a sharp jump (Fig. 7). An examination of the particle configuration shows that the jump occurs when an extra close-packed layer enters $\mathcal{S}$ increasing the number of solid layers by one. For the parameters in our simulation, the jump occurs at $\mu \approx 8$ with the number of layers increasing from 21 to 22. The value of μ at the jump is a strong function of L_s. The solid structure is seen to be a defect-free triangular lattice with a small rectangular distortion $\varepsilon_d(\eta_s, L_s)$ [20]. We have examined the variation of $\Delta\eta(\mu)/\eta$ by cycling μ adiabatically around the region of the jump. This yields a prominent hysteresis loop as shown in Fig. 8, which indicates that "surface" steps (dislocation pairs) nucleated in the course of adding (or subtracting) a solid layer, have a vanishingly short lifetime. Consistent with this we find that the jump in $\Delta\eta(\mu)/\eta$ vanishes when the system is minimized at each μ with a constraint that the solid contains a single dislocation pair (Fig. 8). Interestingly, a dislocation pair forced initially into the bulk, rises to the solid-fluid interface due to a gain in strain energy [37], where they form surface indentations flanked by kink-antikink pairs. This costs energy due to the confining potential; as a result, the kink-antikink pair gets

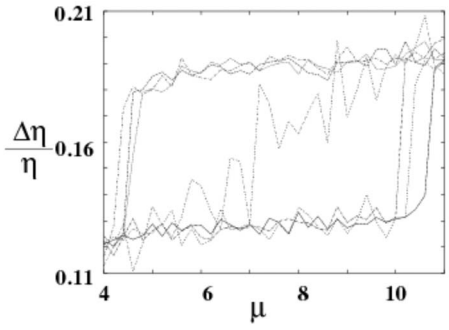

FIG. 8. Hysteresis loop as μ is cycled at the rate of 0.2 per 10^6 MCS. The central jagged line is the result of the initial cycle when a single dislocation pair was present in the solid region.

quickly annihilated by incorporating particles from the adjacent fluid. The jump in $\Delta\eta(\mu)/\eta$ is also seen to decrease with increasing δ_ϕ.

A. Thermodynamic theory

The qualitative features of these results may be obtained by a simple thermodynamic theory (Fig. 7) with harmonic distortions of the solid, ignoring contributions from spatial variations of the density. Note that this theory is in the spirit of a mean field approximation where all effects of fluctuations discussed in the concluding part of the last section are ignored. The free energy of the total system is written down as a sum over the free energies of the solid and the fluid. The free energies of the bulk hard disk fluid and solid are relatively easy to obtain as shown below.

1. Free energy of the solid

In order that the solid channel accommodates n_l layers of a homogeneous triangular lattice with lattice parameter a_0 of hard disks of diameter σ, the channel width

$$L_s = \frac{\sqrt{3}}{2}(n_l - 1)a_0 + \sigma. \tag{4}$$

Defining

$$\chi(\eta_s, L_s) = 1 + \frac{2(L_s - \sigma)}{\sqrt{3}a_0}, \tag{5}$$

if χ=integer=n_l, Eq. (4) is recovered and the channel can accommodate n_l layers of homogeneous triangular lattice and $\chi \neq$ integer implies a rectangular strain away from the perfect triangular lattice. For any given set of values for L_s and η_s one can find χ in the following manner. One can associate a triangular lattice of lattice parameter a_0 from any given $\eta_s = \pi/2\sqrt{3}a_0^2$. This set of a_0 and L_s defines a specific χ. Then the channel can accommodate n_l=int(χ) (nearest integer to χ) number of layers of a centered rectangular (CR) lattice with lattice parameters $a_y = 2(L_s - \sigma)/(n_l - 1)$ and $a_x = \pi/2\eta_s a_y$. This lattice has strains $\varepsilon_{xx} = \frac{n_l - 1}{\chi - 1} - 1$ and $\varepsilon_{yy} = \frac{\chi - 1}{n_l - 1} - 1$. The deviatoric strain $\varepsilon_d = \varepsilon_{xx} - \varepsilon_{yy}$ is then

$$\varepsilon_d = \frac{n_l - 1}{\chi - 1} - \frac{\chi - 1}{n_l - 1}. \tag{6}$$

In the fixed neighbor free-volume theory (FNFVT), particles of high density solid are assumed to be confined within a cage formed by the average positions of its nearest neighbors. This cage and the available free volume of the test particle to move around in this cage is entirely defined by the quantities $b = a_0(1 + \varepsilon_{xx})$ and $h = (\sqrt{3}a_0/2)(1 + \varepsilon_{yy})$ (Fig. 9) [21]. The amount of available free volume $v_{fv}(\eta_s, L_s)$ bounded by the bold line $\mathcal{B}$ in Fig. 9, can be calculated by using tedious but straightforward geometrical considerations. The free-volume free-energy density is $f_s(\eta_s, L_s) = -(4\eta_s/\pi)k_B T \ln(v_{fv})$. f_s always remains an upper bound to the exact free energy. This upper bound becomes asymptotically exact in the close-packed limit. Since ε_{xx} and ε_{yy} have discontinuity at half integral χ, the free-energy f_s has

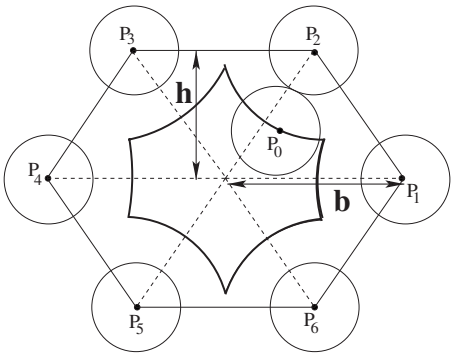

FIG. 9. In our free-volume calculation we assume that the outer six disks are fixed at their average positions and the central disk moves within this cage of fixed particles. The curve in a bold line shows the boundary $\mathcal{B}$ of the free volume available to the central test particle. A point on this boundary is denoted by $P_0(x,y)$, while the centers of the six fixed disks are denoted by $P_i(x_i,y_i)$ with $i=1,2,\ldots,6$. b and h denote the base and the height, which uniquely decides the perimeter of $\mathcal{B}$ and the enclosed free volume. These are functions of density η_s and width of the potential well L_s.

maxima at those χ values [20]. In Sec. VI we present an approximate theory for calculating heat conductance in solid using this free-volume approach [21].

2. Free energy of the liquid

The free-energy density of the liquid bulk phase may be simply written as

$$f_\ell = \rho_\ell \int_0^{\eta_\ell} d\eta'_\ell \frac{P/\rho_\ell - 1}{\eta'_\ell} + f_{id}, \tag{7}$$

where $\rho_\ell = 4\eta_\ell/\pi$, the ideal gas Helmholtz free-energy density $f_{id} = \rho_\ell \ln(\rho_\ell) - \rho_\ell$ and we use the semiempirical equation of state for the hard disk liquid in Ref. [38]. This equation of state has been observed to show excellent agreement with hard disk fluid up to $\eta_\ell = 0.65$ even when the fluid is confined in a hard narrow channel [39]. Following Ref. [38] we use $f_\ell = f_{san} + f_{id}$, where

$$f_{san} = \rho_\ell \frac{(2\eta_c - 1)\ln\left[1 - (2\eta_c - 1)\frac{\eta}{\eta_c}\right] - \ln\left(1 - \frac{\eta}{\eta_c}\right)}{2(1-\eta_c)}, \tag{8}$$

with $\eta_c = \pi/2\sqrt{3}$, the close-packed density for two-dimensional (2D) hard disk triangular lattice.

3. Free energy of the system

We now write down the total free-energy density of the system (fluid+solid regions) using the free-energy density expressions for solid and liquid bulk phases as

$$f = x[f_s(\eta_s, L_s) - 4\eta_s\mu/\pi] + (1-x)f_\ell(\eta_\ell). \tag{9}$$

We then minimize this free-energy density with the constraint that the average density is fixed, $\eta = x\eta_s + (1-x)\eta_\ell$,

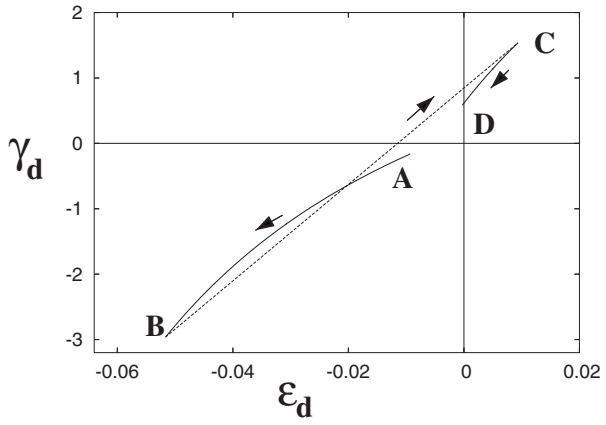

FIG. 10. A plot of the deviatoric stress γ_d against strain ε_d. The arrows show the behavior of these quantities as μ is increased from the points marked A–D. The labels correspond to the same states as in Fig. 7.

where x is the area fraction occupied by $\mathcal{S}$. The result of this calculation is shown in Fig. 7 where it is seen to reproduce the jump in $\Delta\eta(\mu)/\eta$.

Why does the solid incorporate layers of atoms from the liquid? This question may be answered elegantly if one calculates the deviatoric stress γ_d in the solid region as a function of the depth of the strain, ε_d. The stress may in fact be obtained in a straightforward fashion from the expression of the free energy. Differentiating the free energy of the solid with respect to ε_d we obtain

$$\gamma_d = \frac{\partial f_s}{\partial \varepsilon_d}. \tag{10}$$

When γ_d is plotted versus the deviatoric strain ε_d, we observe that the solid is not stress free for any arbitrary combination of μ and L_s. In fact, for our parameters, initially the 21 layered solid is under tension in the y direction. We follow the variation of the deviatoric stress with the strain as μ is increased from the points A–D in the Fig. 10. The state of stress in the solid jumps discontinuously from tensile to compressive from B→C due to an increase in the number of solid layers by one accomplished by incorporating particles from the fluid. This transition is reversible and the system relaxes from a state of compression to tension by ejecting this layer as μ is decreased. As μ is increased, the tension increases till γ_d reaches about −2.96 when the corresponding strain is about −0.052. At this point a layer enters the solid region and the stress and strain switches from tensile to compressive. Further increase in μ now decreases the stress and drives the solid to a state of zero stress at $\mu = 10$. Thus, the layering transition from 21 to 22 layers as observed by us is a mechanism for relieving stress.

In our theory we assumed the channel could accommodate only an integer number of layers and we ignored any possibility of defects. However, our theory allowed for continuous change of base length b. In a small solid, this change is far from continuous. In our FNFVT, while h remains constant until a layering transition, b continuously reduces with

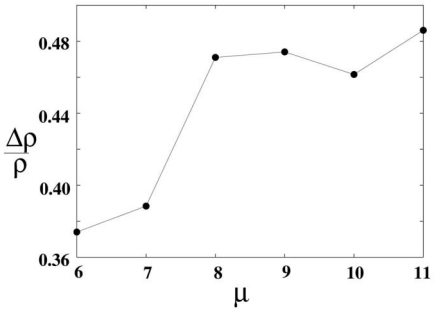

FIG. 11. Plot of the equilibrium fractional density change $\Delta\rho/\rho$ as a function of μ (points—MC data for soft core; the line is a guide to the eye).

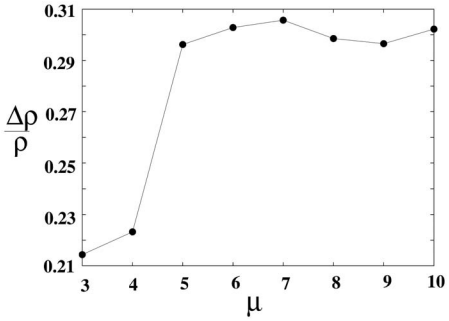

FIG. 12. Plot of the equilibrium fractional density change $\Delta\rho/\rho$ as a function of μ (points—MC data for the Lennard-Jones system; the line is a guide to the eye).

an increase in μ. In reality, b can only be reduced by incorporating a new particle in an existing layer. Once a solid is formed (for $\mu>4$, see Fig. 7), formation of point or line defects are energetically very costly, thus even on an average b can reduce only if all the layers include a particle each and lattice parameters shrink in coherence. This is the reason why in theoretical prediction $\Delta\eta/\eta$ grows smoothly in between the layering transitions, though the same quantity remains almost constant in simulation (Fig. 7). We shall see in later sections that the coherent absorption of particles by all the layers at a time is indeed observed at larger well depth μ in similar simulations with soft core particles.

B. Layering in other potentials

If the layering transition observed in the hard disk system is actually a new mechanism for relieving stress in a thin crystal, it should be independent of the details of the potential. Our main results trivially extend to particles interacting with any form of repulsive potential, or even when the interactions are augmented by a short-range attraction, provided we choose μ deeper than the depth of the attractive potential.

In this section we show explicitly that the layering transition is present in the soft core and Lennard-Jones systems. We choose $k_BT=1$. Once again we perform MC simulations in the constant NAT ensemble with periodic boundary conditions and with the external chemical potential μ. The relevant parameters corresponding to these potentials, namely, ϵ and σ in $u^{SS}(r)=\epsilon\left(\frac{\sigma}{r}\right)^{12}=ar^{-12}$ and $u^{LJ}(r)=4\epsilon\left[\left(\frac{\sigma}{r}\right)^{12}-\left(\frac{\sigma}{r}\right)^{6}\right]$, set the energy scale and the length scale, respectively. Here $r=r_{ij}$ is the distance between the pair of atoms i, j. In our simulation $\epsilon=\sigma=1$ and $N=1200$ particles occupy an area $A=24\times 60$ with the solid occupying the central third of the cell of size $L_s=20$. The average density of the system is therefore kept at $\rho=0.833$, which is to be compared with the freezing densities $\rho\simeq 0.987$ [40] and $\rho\simeq 0.865$ [41] for the soft core (Fig. 11) and Lennard-Jones (Fig. 12) systems, respectively. For the soft core potential, the μ value at the jump in density (Fig. 11) is even quantitatively comparable to the corresponding hard core system. In soft core systems the other possible mode of stress relaxation, namely, coherent inclusion of one particle each in all the existing layers is observed at a larger well depth of $\mu\approx 16$. We shall discuss this further in Sec. VI while discussing heat transport in this soft core system.

IV. KINETICS OF LAYERING

The large hysteresis loops associated with the layering transition obtained in the last section makes it clear that the kinetics of this transition is slow. To study the lifetime of the kink-antikink pairs (surface step), we resort to an MD simulation, using a velocity Verlet algorithm [17], with the unit of time given by $\tau=\sqrt{m\sigma^2/k_BT}$, where $m(=1)$ is the mass of the hard disks. Using values of m and σ typical for atomic systems like Ar or Rb, $\tau\approx 1$ ps. A time step of $\Delta t=7\times 10^{-5}\tau$ conserves the total energy to within 1 in 10^3 (at worst).

Starting with an equilibrium configuration for the hard disk system, taken from our MC runs as discussed in Sec. II at $\mu=9.6$ corresponding to a 22-layer solid, we create a unit surface step of length l by displacing a few interfacial atoms from the solid region into the liquid and "quench" across the transition to $\mu=4.8$, where a 21-layer solid is stable. The rest of the parameters are kept identical to those given in Sec. II. We observe that the fluctuation thus created rapidly relaxes back and the surface step vanishes as the atoms are pulled back into the solid. We illustrate this by plotting the number of hard disks within the solid region as a function of the MD time steps (Fig. 13). As soon as a step is created, the line of atoms in the portion of the solid thus exposed bend to fill up the gap created between the atomic layers and the edge of the

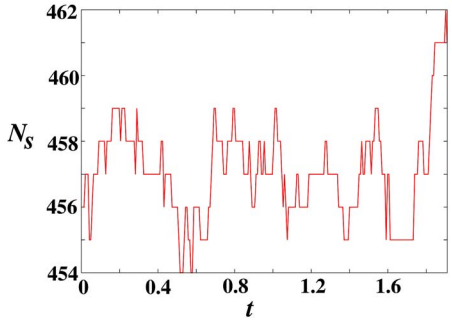

FIG. 13. (Color online) Plot of the number of particles in the solid region N_s as a function of time t (in units of τ) clearly shows that the displaced particles are pushed back into the region $\mathcal{S}$.

potential trap. This generates considerable local elastic stress. Also, the liquid layer lying immediately adjacent to the solid has a lot of orientational and solidlike order. For short times it responds elastically to the presence of an increased local density of atoms. The combined elastic response therefore pushes the displaced atoms back into the solid region thereby annihilating the step. This annihilation is a transient response and happens within a time of τ, whereas the lifetime of the metastable 22-layered solid is about 10τ, which is one order of magnitude larger. Indeed, a free-energy audit involving a bulk-free energy gain $\Delta F \sim 1/L_s$, going from a 22- to a 21-layered solid, and an elastic energy cost $\sim \ln(l)$ for creating a step of size l, reveals that a surface step is stable only if $l \geq l^* \sim 1/L_s$. For small L_s, the critical size l^* may therefore exceed L_x, the total length of the interface. Of course, if the step spans the entire length of the interface, there is no bending of the atomic lines and there is no elastic energy cost. This explains the slow kinetics since the system has to wait until a rare random fluctuation, which displaces all the atoms in a solid layer across the interface coherently, gives rise to layering transition. Although we have explicitly demonstrated this for the hard disk system, we believe that similar considerations should be appropriate for the soft disk and Lennard-Jones systems too.

The slow kinetics of the layering transition may have an impact on the transfer of momentum across the liquid-solid interface in the form of regular sound waves or acoustic shocks. The large effective compressibility of the solid at the layering transition as evidenced by the jump in the density as the chemical potential is increased by an infinitesimal amount (Fig. 8) should reduce the velocity of sound considerably. The propagation and scattering of sound in an inhomogeneous region with coexisting phases has been studied extensively [42–45] in the past. The transfer of mass between coexisting phases at interphase boundaries is known to slow down and dissipate sound waves traveling through the system. Our system has an artificially created inhomogeneity, which should have a similar effect on its acoustic properties.

Further, the mechanism of stress relaxation of a thin (L_s small) solid via the transfer of an entire layer of atoms may be exploited in a variety of practical applications, provided we can eject this layer of atoms deep into the adjoining fluid and enhance its lifetime. We may be able to use the ejected layer of atoms to create monolayer atomic films or coatings [46]. Highly stressed monoatomic layers tend to disintegrate or curl up [47] as they separate off from the parent crystal. It may be possible to bypass this eventuality, if the time scale of separation is made much smaller than the lifetime of the layer. Can acoustic spallation [24] be used to cleave atomic layers from a metastable, stressed nanocrystal?

In the next section, therefore, we study the response of the liquid-solid interface in our system of hard disks to acoustic shocks with a view to studying the effect of the layering transition on acoustic shock propagation and dissipation as well as the properties of the ejected layer.

V. MASS AND MOMENTUM TRANSFER

Consider sending in a sharp laser (or ultrasonic) pulse, producing a momentum impulse $[v_y(t=0)=V_0]$ over a thin region in y spanning the length L_x of the simulation cell. This results in a weak acoustic shock [24] (corresponding to a laser power $\approx 10^2$ mW and a pulse duration 1 ps for a typical atomic system). The initial momentum pulse travels through the solid and emerges at the far end (Fig. 14) as a broadened Gaussian. The width of this Gaussian pulse, Δ, is a measure of absorption of the acoustic energy of the pulse due to combined dissipation in the liquid, the solid, and at the interfaces [42,43,48]. For large enough pulse strengths V_0, this is accompanied by a *coherent* ejection of the (single) outer layer of atoms into the fluid. Note that in our MD simulations, to reduce interference from the reflected pulse through periodic boundary conditions, we increase the fluid regions on either side, so that for the MD calculations we have a cell of size 22.78×186.98 comprising 3600 particles. This is accomplished by separately equilibrating two liquid regions of appropriate size and density and smoothly sandwiching our equilibrated system (which includes the solid strip) in between these liquid regions. The whole 3600 particle system is equilibrated for a further 10^4 MCS before it is used as an initial condition for the MD simulations. In Fig. 14 we show the initial momentum pulse with strength $V_0=6$, as produced within a narrow strip of size $\sim\sigma$, just to the left of the solid region and the curves are fitted to a Gaussian (and the width Δ^2 extracted) when the maximum of the pulse reaches a fixed distance of 44.1 from the source. A reflected pulse can also be seen.

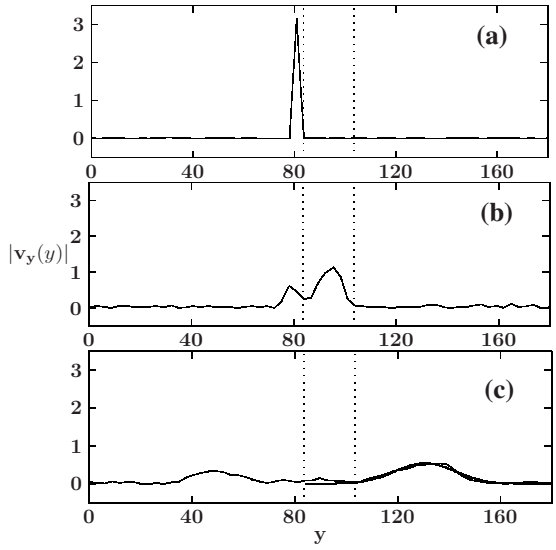

FIG. 14. [(a)–(c)] Plot of the absolute value of the momentum $|v_y(y)|$ for molecular dynamics times $t=0.0007$ (a), 0.2828 (b), and 2.8284 (c). The dotted lines show the position of the solid-fluid interfaces. The fit to a Gaussian (thick solid line) is also shown in (c). Curves such as in (a)–(c) are obtained by averaging over 100–300 separate runs using different realizations of the initial momentum (figure reproduced from Ref. [15]).

When a shock wave, which propagates through a conventional solid, emerges from the free surface, the compressed material expands—or unloads—to zero pressure [24]. The unloading (rarefaction) wave travels backwards into the material with the speed of sound. The response of the solid depends on the specific nature of the shock front. For a shock

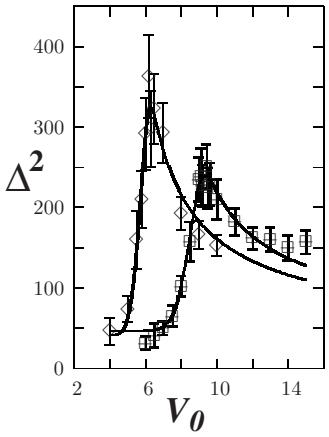

FIG. 15. Plot of the squared width Δ^2 of the momentum pulse after it emerges from the solid as a function of V_0 for μ=4.8 ($\diamond$) and 9.6 ($\square$). The solid lines are fits to an effective liquid theory. The peak in $\Delta^2(V_0)$ so produced is more prominent for the metastable 22-layered solid μ=4.8 than for the stable (μ=9.6) system showing a more coherent momentum transfer in the former case (figure reproduced from Ref. [15]).

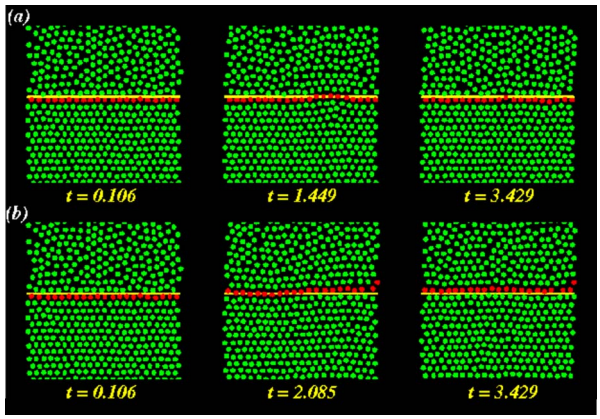

FIG. 16. (Color online) (a) Configuration snapshot from a portion of our MD cell showing hard disk atoms (green circles) at the solid- (bottom) liquid interface (yellow line) as a weak momentum pulse (V_0=2) emerges into the liquid, at three different times, for μ=4.8. The pulse initially ejects a few atoms from the solid but are subsequently pulled back due to the large elastic strain cost in bending of the interfacial crystalline layer (red circles). (b) The same for a stronger momentum pulse V_0=6. This time the pulse strength is sufficient to eject the layer.

wave with an approximately Gaussian profile as in our case, significant negative pressures can develop at the interface where the shock emerges due to the interaction of the forward and the reflected waves and a portion of the solid may split off by a process known as "spallation." Spallation in bulk solids like steel needs acoustic pressures in excess of 10^5 N/cm^2 [24] usually available only during impulsive loading conditions; the ejected layer is a "chunk" of the surface. In contrast, the pressures generated by the shock wave in our system causing coherence *nanospallation* involves much smaller surface stresses of the order $k_BT/\sigma^2 \approx 10^{-5}$ N/cm^2. This difference comes about because unlike a bulk system, a strained nanocrystal on the verge of a transition from a metastable $n+1$ to a n layered state readily absorbs kinetic energy from the pulse. Also, as mentioned before, a confined solid strip in two dimensions has very strong smectic ordering, which effectively decreases the coupling between the layers [20,35]. In fact, a quasi-one-dimensional solid ($L_x \gg L_s$) is better regarded as a smectic with weak solidlike modulations. The fact that surface indentations are unstable (Fig. 16) unless of a size comparable to the length of the crystal L_x, ensures that a full atomic layer is evicted almost always, leading to coherent absorption of the pulse energy. The coherence of this absorption mechanism is markedly evident in a plot of Δ^2 against V_0, which shows a sharp peak (Fig. 15). Among the two systems studied by us, viz., a metastable (μ=4.8) and a stable (μ=9.6) 22-layered solid, the former shows a sharper resonance. Note that the absorption of momentum is largest when the available kinetic energy of the pulse exactly matches the potential energy required to eject a layer. To elucidate this fact further, we plot the configurations of the metastable system (μ=4.8) as the pulse travels through the system, for two different pulse strengths V_0=2 and V_0=6 (Fig. 16). The weaker momentum pulse (V_0=2) initially ejects a few atoms of the interfacial crystalline layer of the metastable 22-layered solid. However, the resulting large nonuniform elastic strain evidenced by the bending of lattice layers causes these atoms to be subsequently pulled back into the solid. This effect is the same as that seen in the last section. Only a stronger pulse V_0=6, capable of ejecting a complete lattice layer, succeeds in reducing the number of solid layers by one leading to an overall lower elastic energy.

The eviction of the atomic layer is therefore assisted by the strain-induced interlayer transition and metastability of the 22-layered solid discussed above. Spallation is also facilitated if the atomic interactions are anisotropic so that attraction within layers is stronger than between layers (e.g., graphite and layered oxides [47]), for our model of purely repulsive hard disk solid, an effective intralayer attractive potential of mean force is induced by the external potential [20].

The spallated solid layer emerges from the solid surface into the fluid, and travels a distance close to the mean free path, whereupon it disintegrates due to viscous dissipation (Fig. 17). A simple estimation of the lifetime of the ejected layer may be undertaken as follows. To obtain the lifetime of the spallated layer we obtain the time development of the Fourier component of the local density correlation $\langle \psi_{\mathbf{G}_2}(y) \rangle$, which is just a time-dependent generalization of the quantity shown in Fig. 5. We obtain this by averaging, at each time slice t, the quantity $\Sigma_{\langle i,j \rangle} \exp[-i\mathbf{G}_2 \cdot (\mathbf{r}_i - \mathbf{r}_j)]$ over all nearest neighbor pairs $\langle i,j \rangle$ with the center of the vector $(\mathbf{r}_i - \mathbf{r}_j)$ lying within a strip of width $\sim\sigma$ centered about y and spanning the system in x. The wave number $\mathbf{G}_2 = (2\pi/d)\hat{\mathbf{n}}$, where d=0.92 is the distance between crystal lines in the direction $\hat{\mathbf{n}}$ normal to the fluid-solid interface. The solid (central region with $\psi_{\mathbf{G}_k}(y,t) \neq 0$, for k=1,2,3) ejects a layer (shown by an arrow in Fig. 17), which subsequently dissolves in the fluid. The lifetime of the layer is around 2–3 time units (τ),

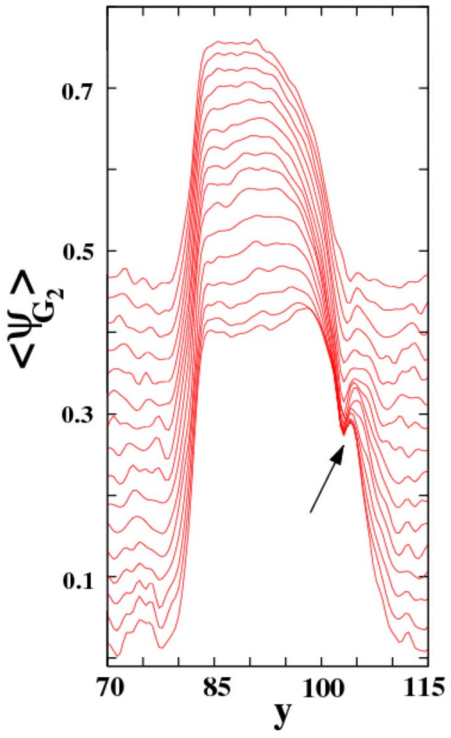

FIG. 17. (Color online) A plot of the time development $\langle\psi_{G_2}(y)\rangle$. The solid ejects a layer (shown by an arrow), which subsequently dissolves in the fluid. The curves from bottom to top correspond to time slices at intervals of $\Delta t=0.07\tau$ starting from $t=1.06\tau$ (bottom). We have shifted each curve upward by $0.03t/\Delta t$ for better visibility (figure reproduced from Ref. [15]).

which corresponds to a few ps for typical atomic systems. The lifetime increases with decreasing viscosity of the surrounding fluid. Using the Enskog approximation [49] to the hard disk viscosity, one can calculate the bulk viscosity for a hard disk fluid to be [49,50]

$$\zeta_E = \frac{16}{\pi}\zeta_{00}\eta^2 g(\sigma), \tag{11}$$

where ζ_{00} is a constant and $g(\sigma)$ is the pair-correlation function at contact. For a system of hard disks with $m=\sigma=\beta=1$, $\zeta_{00}=1/2\sqrt{\pi}$ [50]. Thus, $\zeta_E \propto \eta^2$ and we estimate that by lowering the fluid density one may increase the lifetime of the layer considerably. The lifetime enhancement is even greater if the fluid in contact is a low density gas (when the interparticle potential has an attractive part [51]).

A. Effective liquid theory

The absorption line shape may be understood within a phenomenological "effective liquid" approximation. The extra absorption producing the prominent peak in Fig. 15 is due to the loss of a whole layer from the solid into the liquid (Fig. 16). For small V_0, the confined solid responds by center of mass fluctuations ($q\to 0$ phonons) shown by oscillations of N_s with time (Fig. 18).

Scattering from this and other sources [42–45,48] constitute a background which we ignore, as a first approximation,

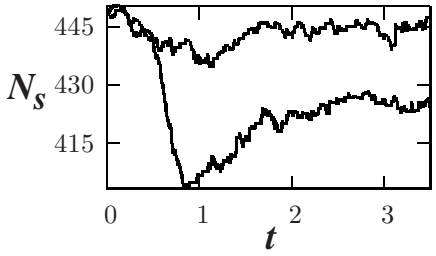

FIG. 18. A plot of the total number of particles N_s within the solid region ($\mu=4.8$) as a function of time for $V_0=1$ (top) and 6. Note oscillations in N_s; only the stronger pulse changes the number of solid layers from 22 to 21.

for simplicity. Within our approximation, the momentum loss at the interface is modeled as regular dissipation within a liquid strip of (fictitious) width ξ. The expected momentum transfer at the interface $\Pi_e=\Pi_0\times$ the probability that the momentum Π_0 required to eject the layer, exists (see Fig. 19). If a local "temperature" T_{local} measures the degree of (de)coherence of the momentum transfer, then $\Pi_e=(1/2)\Pi_0\,\mathrm{erfc}[(\Pi_0-V_0)/\sqrt{2k_BT_{local}}]$ and ξ may be extracted from $V_0-\Pi_e=V_0\exp(-\alpha\omega^2\xi)$. Substituting for Π_e we obtain the extra absorption due to the interface

$$\Delta^2 = 4\alpha c_0^2\xi = -a\ln\left[1-\frac{\Pi_0}{2V_0}\,\mathrm{erfc}\left\{\frac{\Pi_0-V_0}{\sqrt{2k_BT_{local}}}\right\}\right]. \tag{12}$$

We use a, Π_0, and T_{local} as fitting parameters. In Fig. 15 we show a fit to Eq. (12) of our MD data and observe that it reproduces all the features remarkably well. The larger error bars near the peak in $\Delta^2(V_0)$ reflects the difficulty of fitting a Gaussian to the transmitted pulse when dissipation is large. Indeed, in this region the pulse shape is systematically distorted away from Gaussian due to effects beyond the scope of our simple theory. Large fluctuations in N_s (Fig. 18) lead to an expected [42–45] and detectable decrease in average pulse speed (Fig. 20).

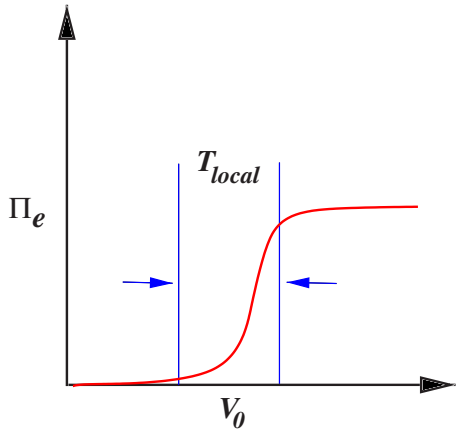

FIG. 19. (Color online) A schematic diagram showing the momentum transfer as assumed in our phenomenological theory.

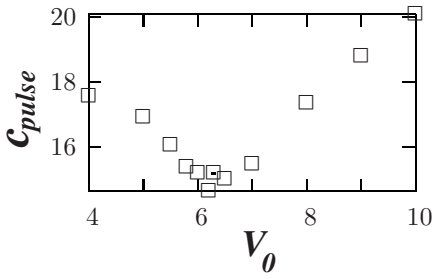

FIG. 20. Average pulse velocity $c_{pulse}(V_0)$ for $\mu=4.8$; note the dip in c_{pulse}, where absorption is strongest.

VI. HEAT TRANSPORT

In this section we focus on the transport of energy across the system of forced solid in contact with its own liquid. The heat conductivity λ is defined by the celebrated Fourier's law $\mathbf{j}_E=-\lambda\nabla\mathbf{T}$, where $\mathbf{j}_E$ is the heat current density and $\nabla\mathbf{T}$ is the temperature gradient. The transport of heat through small and low dimensional systems has enormous significance in the context of designing useful nanostructures [48]. A large number of recent studies in lower dimensions has shown that heat conductivity is, in fact, divergent as a function of system size [52–54]. Thus it is more sensible to calculate the heat current or conductance of the system directly, rather than the heat conductivity. Therefore we focus on the heat current densities j_E (>0) flowing across the solid-liquid interface from high to low temperature and heat conductance $G=j_E/\Delta T$ (or resistance $R=1/G$), ΔT (>0) being the temperature difference between the two edges of a given region. In this study, we are particularly interested in exploring the impact of structural changes, viz., the layering transitions, on heat transport. This is to remember that, layering transitions are strongly dependent on the small system sizes and gets washed away as one goes to larger systems. Recently, electrical [55] and thermal transport [21] studies on confined solid strips have revealed strong signatures of structural transitions due to imposed external strain. Heat transport across a model liquid-solid interface has been studied in three dimensions with the interatomic potential being Lennard-Jones [25]. In Ref. [25] it is shown that the Kapitza resistance [26], the interfacial resistance, can reach appreciably large values when the liquid does not wet the solid.

A. Nonequilibrium molecular dynamics

The specific context in which we study thermal properties of the liquid-solid interface is the same as that we have used for our studies of the acoustic properties in the last section. Again, a solid region is created within a liquid using an external chemical potential trap. We report results for 1200 particles interacting via the soft disk potential $u(r_{ij})=1/r_{ij}^{12}$ taken within an area of 24×60. In the absence of any external potential, a 2D system of soft disks at this density $\rho\approx 0.65$ remains in the fluid phase. The length scale is set by soft disk diameter $d=1$, energy scale by temperature k_BT, and the time scale by $\tau_s=\sqrt{md^2/k_BT}$. The unit of energy flux j_E is thus set by $(k_BT/\tau_s d)$. The unit of resistance and conductance are $\tau_s d$ and $(\tau_s d)^{-1}$, respectively. The smooth interaction potential allows us to use standard MD simulations with a velocity Verlet algorithm. The time step of $\delta t=10^{-3}\tau_s$ in our MD ensures that the total energy is conserved (in equilibrium) to within 10^{-4}. Periodic boundary conditions are applied in the x direction. We use the standard velocity Verlet scheme of MD with equal time update of time step δt, except when the particles collide with the "hard walled" heat reservoirs at $y=0$ and $y=L_y$. We treat the collision between the particles and the reservoir as that between a hard disk of unit diameter colliding against a hard structureless wall. If the time τ_c of the next collision with any of the two reservoirs at either end is smaller than δt, the usual update time step of the MD simulation, we update the system with τ_c. During the collision with the walls Maxwell boundary conditions are imposed to simulate the velocity of an atom emerging out of a reservoir at temperatures T_L (at $y=0$) or T_R (at $y=L_y$) [53]. This means that whenever a soft disk collides with either the left or the right wall it gets reflected back into the system with a velocity chosen from the distribution

$$f(\vec{v})=\frac{1}{\sqrt{2\pi}}\left(\frac{m}{k_BT_W}\right)^{3/2}|v_y|\exp\left(-\frac{m\vec{v}^2}{2k_BT_W}\right), \qquad (13)$$

where T_W is the temperature (T_L or T_R) of the wall on which the collision occurs. During each collision energy is exchanged between the system and the bath. Thus in our molecular dynamics simulation, the average heat current flowing through the system can be found easily by computing the net heat loss from the system to the two baths (say Q_L and Q_R, respectively) during a large time interval τ, once the system has reached steady state. The steady state heat current from right to left bath is given by $\langle J\rangle=\lim_{\tau\to\infty}Q_L/\tau=-\lim_{\tau\to\infty}Q_R/\tau$. In the steady state the heat current (the heat flux density integrated over x) is independent of y. This is a requirement coming from current conservation. For a homogeneous system $j_E=\langle J\rangle/L_x$. However, if the system has inhomogeneities then the flux density itself can have a spatial dependence and in general we can have $j_E=j_E(x,y)$. In our simulations we have looked at $j_E(x,0)$ and $j_E(x,L_y)$.

B. Results

In Fig. 21 we show that even in the presence of a temperature difference across the system, the solid-liquid interface is formed and the liquid near the interface shows smecticlike density modulation due to the presence of a nearby solid. These features are apparent from the structure factor calculated outside the region $\mathcal{S}$ (liquid), inside the region $\mathcal{S}$, and in the small region over which external potential goes to the value $-\mu$ from zero [Fig. 21(a)]. The local density profile also shows constant large value corresponding to the solid formed in region $\mathcal{S}$ [Fig. 21(b)]. The density of the liquid near the cold $(k_BT=0.5)$ left reservoir is higher than the density of liquid near the hot $(k_BT=1.5)$ right reservoir. In Fig. 21(c) we plot the local compressibility $\kappa_T(y)$ defined via $\kappa_T=\rho^{-2}(\partial\rho/\partial\mu)_T$. The compressibility of the interfaces is very large making the narrow solid region also unusually compressible pointing to the presence of large local number fluc-

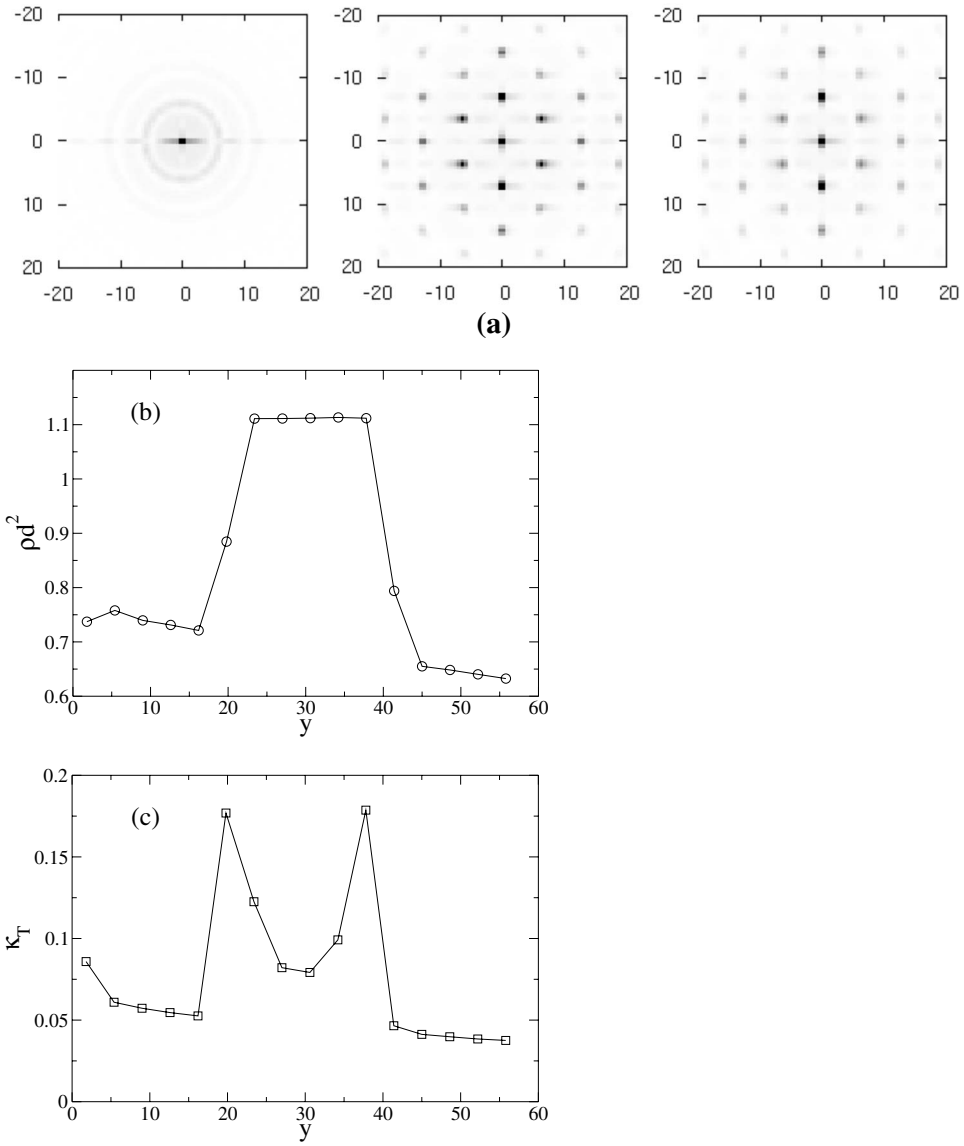

FIG. 21. (a) From left to right, structure factors in liquid, solid, and interface regions. Interface shows clear smectic profile. Data taken at $\mu=13$. (b) The local density profile along the y direction at $\mu=13$. (c) The isothermal compressibility κ_T as a function of y at $\mu=13$. Compressibility shows strong peaks near the interfaces. Due to small size, interfacial enhancement of compressibility permeates right through the whole of the solid region. In (b) and (c) the lines are guides to the eye. [Figures (b) and (c) were reproduced with permission from Journal of Physics: Condensed Matter [16]].

tuation. This behavior helped in large shock absorption as discussed in Sec. V. Before going into the details of heat transport in this system, let us first enlist some details of the structural transitions obtained. With an increase in the strength of the trapping potential, both in equilibrium and in nonequilibrium situations, we observe two modes of density enhancement: (a) A whole layer of particles enters to increase the number of lattice planes in the y direction. This happens, e.g., as μ is increased from 7 to 8. Thus in this mode the interlattice plane separation decreases [see Fig. 22(a)]. (b) Each of the lattice planes grow by one atom thereby decreasing the interatomic separation within a lattice plane. This happens, e.g., as one increases μ from 10 to 12 [see Fig. 22(c)]. In the intermediate configurations one observes metastable dislocation pairs [Fig. 22(d)] and peaks in the local particle density that hops back and forth between two neighboring positions [Fig. 22(b)] to maintain commensurability. In the mode (a) one observes a sudden compression in the y direction associated with positive ε_d and γ_d, while in the mode (b) the system undergoes tension associated with negative ε_d and γ_d. With an increase in μ, these two modes repeat one after another, in cycle. This allows the system to release the extra stress developed in one direction due to particle inclusion in the previous cycle by the inclusion of a particle in the other direction in the next one. Certainly, at large enough μ the solid region goes towards very high packing fraction, thereafter stopping the process of particle accumulation. To summarize the major structural changes obtained in soft disk solid, we find, strained triangular solids with 23×23, 24×23, 24×24 unit cells at $\mu=8$, 12, and 24 respectively (see Fig. 22). The large elastic and core energy cost inhibits the formation of an equilibrium nano solid with dislocations—even if dislocations form, the solid eventually gets rid of them by either incorporating particles from or ejecting them to the liquid part.

Before any measurement is done, the system is allowed to reach the steady state where the current density integrated over the whole x range is the same at all y. If LTE is maintained, $v(y)$ is expected to obey Gaussian distribution locally. That gives definitions of local temperature from all the even

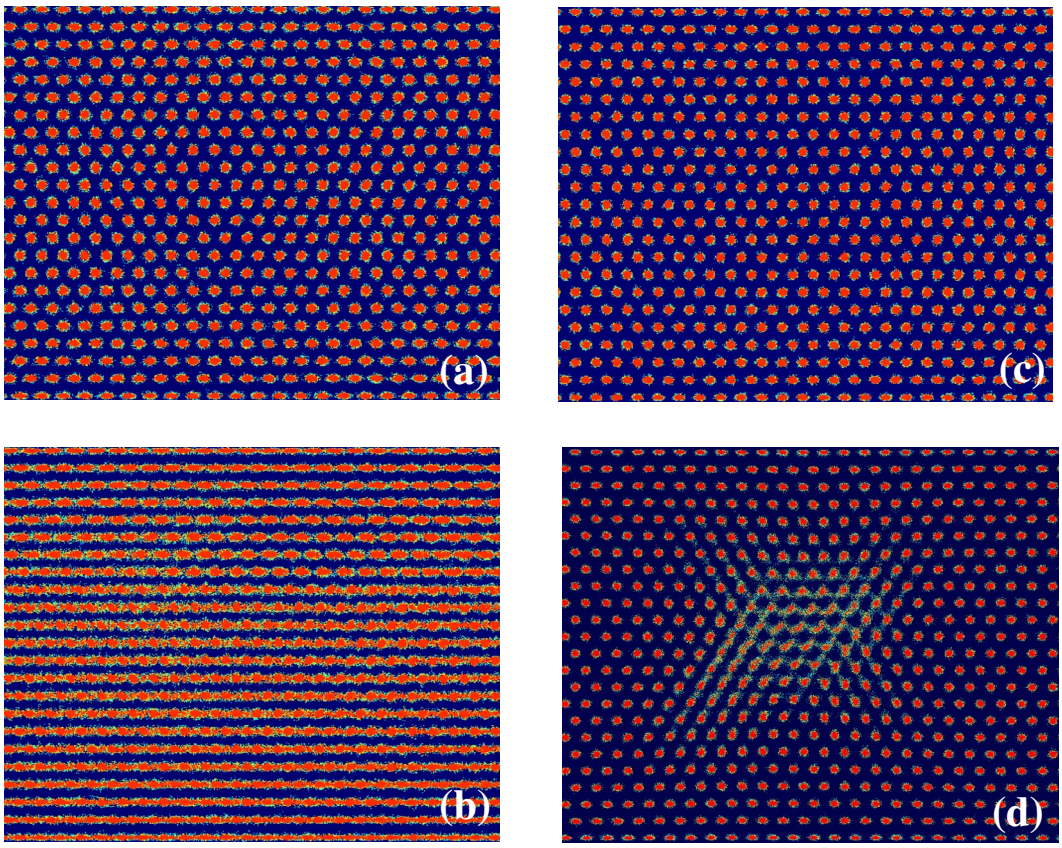

FIG. 22. (Color online) Overlapped density plot of 500 configurations in the region trapped by external potential μ: (a) A 23×23 triangular lattice solid at $\mu=8$. (b) Local density peaks hop in the x direction to incorporate >23 particles in lattice planes in response to increased potential $\mu=11$. (c) A 24×23 triangular lattice solid at $\mu=12$. Notice the increase in particle numbers in the lattice planes. (d) Configuration obtained after $15\,000\delta t$ as a 24×23 steady state solid at $\mu=16$ is quenched to $\mu=24$. This shows a dislocation pair—a 23-layered region trapped in between a 24-layered solid. At steady state (after a time $10^5\delta t$) dislocations annihilate to produce a 24×24 triangular lattice solid. Color code: blue (dark): low density and red (light): high density (figure reproduced with permission from Journal of Physics: Condensed Matter [16]).

moments of $v(y)$. Thus $k_BT(y)=\langle 1/2mv^2(y)\rangle$ and $k_BT(y)=m\sqrt{\langle v^4(y)\rangle}/8$, etc. To check for the local thermal equilibrium (LTE) from our simulation, we find $\langle v^2(y)\rangle$ and $\langle v^4(y)\rangle$ as a function of distance y from cold to hot reservoir and compare the above mentioned definitions of $k_BT(y)$ [Fig. 23(a)]. From Fig. 23(a) it is evident that the temperature profile is almost linear in the single phase regions, such as the liquid and the solid, with a sharp increase near the interfaces and the LTE is approximately valid in all regions. In Fig. 23(b) we plot temperature profiles $k_BT(y)$ as obtained from $\langle 1/2mv^2(y)\rangle$ at well separated trapping potentials $\mu=8,16,21$. With increased trapping strength, the temperature difference between the edges of the solid region decreases indicating an enhancement of heat conductance within the solid. The temperature jumps at the interfaces also increase with increasing trapping potential. Such a jump in the temperature is known as the Kapitza or contact resistance (R_K) [26]. This is defined as

$$R_K=\frac{\Delta T}{j_E}, \tag{14}$$

where ΔT is the difference in temperature across the interface. It is evident that the interfaces are the regions of the highest resistance in the system. This large resistance can be traced back to large density mismatch at the contact of two phases. The conductance of the high temperature liquid near the right reservoir with $k_BT_R=1.5$ is lower than the low temperature liquid in the other side in contact with the reservoir with $k_BT_L=0.5$. The temperatures are expressed in units of k_BT. The heat current, as expected, flows from the right reservoir to the left reservoir.

In Fig. 24 we have plotted the heat flux through the system as a function of μ. As μ increases, the atoms from the surrounding liquid get attracted into the potential well and the density of the solid progressively becomes higher at the cost of the liquid. Because of Kirchoff's law, the heat conductance of a composite system of liquid-solid-liquid connected in series through interfacial regions is dictated by the low conductance regions. The decrease in liquid density decreases the pressure in the liquid regions, thereby reducing the heat conductance in them [56]. The conductance in liquid is always lower than in solid. These result in an overall decrease in the heat flux and consequently, the overall conductance. Moreover, at larger μ there occurs larger density mismatch at the interfaces leading to larger Kapitza resistance (Fig. 26). The change in density is sharper near the two layering transitions—thus heat flux shows sharper drops near

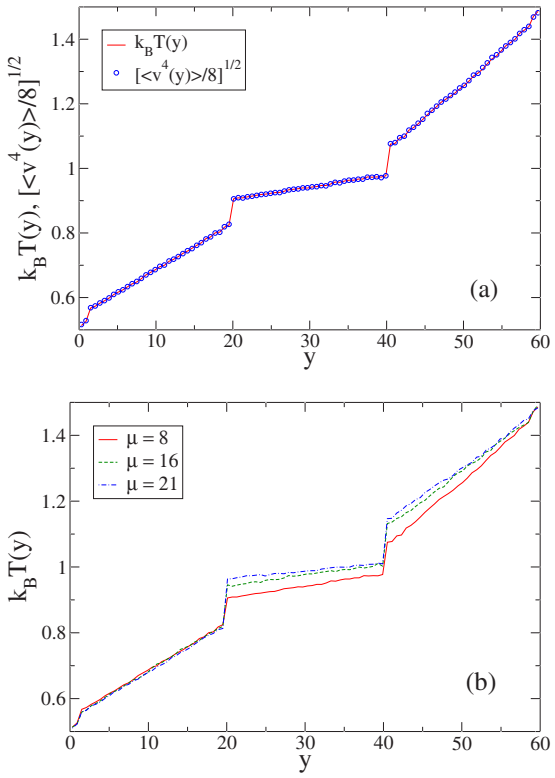

FIG. 23. (Color online) (a) Plot of temperature profile $\langle 1/2mv^2(y)\rangle$ and $m\sqrt{\langle v^4(y)\rangle}/8$ at $\mu=8$. (b) The temperature profile $\langle 1/2mv^2(y)\rangle$ as a function of y, the system coordinate perpendicular to the reservoirs, for $\mu=8,16,21$ [Figure (a) reproduced with permission from Journal of Physics: Condensed Matter [16]].

the transitions at $\mu=7-8$ and $\mu=11-12$. However, close to the layering transition at $\mu\sim 8$ there is a local peak in the value of the heat flux suggesting that a significant amount of kinetic energy is exchanged between the liquid and solid through the interface at the layering transition. This excess conduction is due to an enhanced number fluctuation in the direction of heat flow in this mode of layering transition.

In Fig. 25 we show the heat conductance in solid region G_s as a function of strength of the trapping potential μ. The

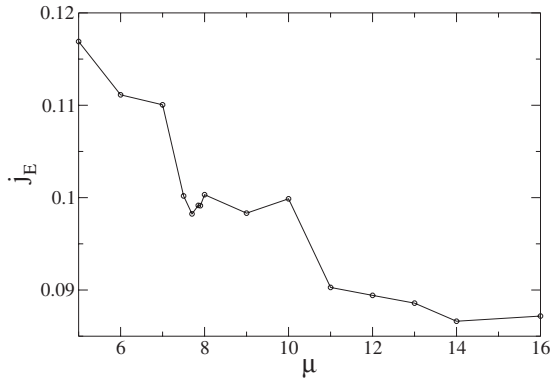

FIG. 24. Plot of the heat flux j_E as a function of the trap depth μ. Note that the overall flux decreases as a function of μ. j_E is expressed in units of $k_BT/\tau_s d$ (figure reproduced with permission from Journal of Physics: Condensed Matter [16]).

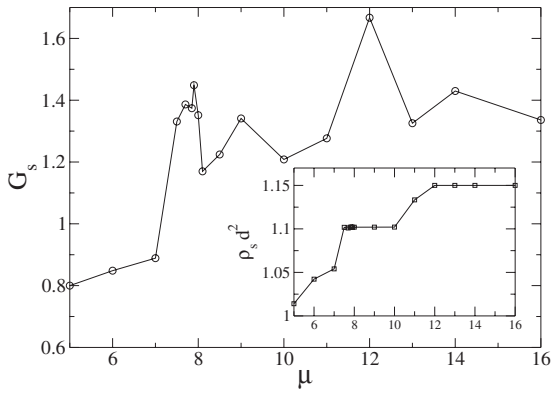

FIG. 25. Plot of the thermal conductance of the solid region G_s as a function of μ. G_s is plotted in units of $(\tau_s d)^{-1}$. The inset shows change in solid density $\rho_s d^2$ as a function of μ. Jump increase in $\rho_s d^2$ associated with layering shows up in a sudden large increase in conductance near $\mu=7.5$. Another sharp increase in $\rho_s d^2$ near $\mu=12$ is due to growth of lattice planes by one atom each; this happens in the orthogonal direction to heat conduction and does not affect G_s (figure reproduced with permission from Journal of Physics: Condensed Matter [16]).

inset in Fig. 25 shows the change in the averaged density of the solid region $\rho_s d^2$. The $\rho_s d^2-\mu$ plot shows clear staircaselike sharp increases near $\mu=8,12$. As μ is increased from 7 to 8, a layering transition in a direction perpendicular to the interfaces occurs; whereas as μ is increased from 10 to 12 each of the lattice planes lying parallel to the solid-liquid interfaces grows by one atom [see also Figs. 22(a) and 22(c)]. These two modes of density fluctuations leave their signatures by enhancing heat conductance G_s. Notice that, the layering transition at $\mu=8$ increases stress in the solid region in the direction of heat conduction, thereby showing a steplike increase. The other mode of density fluctuation is in the normal direction to heat transport and thereby affects the heat conductance only near the transition due to the associated enhancement of overall fluctuations (a sharp peak at $\mu=12$).

We now find out the Kapitza resistance across the solid-liquid interface as a function of the strength of the external potential μ. With an increase in μ, the system shows a jump in the density of the solid region corresponding to the addition of an entire layer of atoms (see inset of Fig. 25). From the profile shown in Fig. 23(b), the Kapitza resistance is easily obtained by dividing the temperature jump by the energy flux. Note that a slight dependence of R_K on T is visible in Fig. 23(b) with a larger temperature jump on the "warm" side. The results shown in Fig. 26 correspond to the average values of R_K over the "warm" and "cold" sides.

The plot of R_K as a function of μ shows a distinct jump as a layer is included (for a value of μ close to 8) in the solid region (Fig. 26). The jump in R_K is also accompanied by a local dip at the transition, corresponding to larger number fluctuations at the interface. The combined effect of the enhanced Kapitza resistance as well as enhanced conductance of the solid can be summarized by defining the Kapitza length in units of width of the solid region L_s as $l_K=R_K G_s$. This is a measure of excess width of a solid, which is equiva-

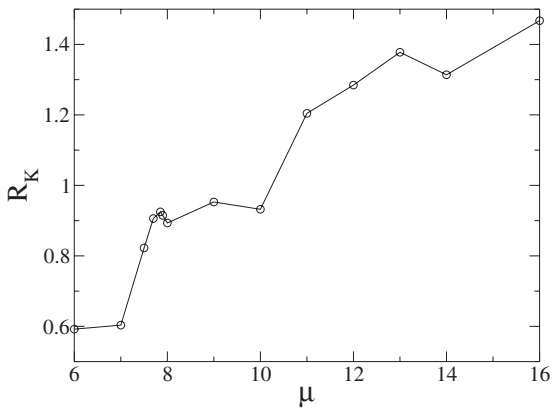

FIG. 26. Plot of the Kapitza resistance, R_K, expressed in units of $\tau_s d$ as a function of μ, shows a jump at the layering transition (figure reproduced with permission from Journal of Physics: Condensed Matter [16]).

lent in giving rise to a resistance equal to the Kapitza resistance. This is reminiscent of the "effective liquid" concept, which has been used in explaining some of the features of acoustic shock absorption in the last section. The Kapitza length also shows a peak near the layering transition at $\mu=12$ (Fig. 27).

The layering transitions in solid occur via dislocation formation, which ultimately annihilates by incorporating more particles from the liquid region. The kinematics of dislocation formation and annihilation is assisted by diffusion and dislocation climb, which are very slow processes [20] in a solid compared to particle collision and kinetic energy transfer times. Thus it is possible for a system with metastable dislocation pairs to reach a thermal quasisteady state. Figure 22(d) shows overlapped configurations of the solid region containing a dislocation-antidislocation pair, as the system is quenched from $\mu=16$ to $\mu=24$. The overlapped configurations are separated by time $100\delta t$ and collected after a time of $15\,000\delta t$ after the quench begins. Since dislocations annihilate though a conserved diffusive dynamics, which takes a long time ($10^5\delta t$) compared to the particle collision and kinetic energy transfer times, the system in the presence of dislocation pairs is in an effective steady state. It also maintains LTE that we have checked by computing $\langle v^4(y)\rangle$ and $\langle v^2(y)\rangle$ locally. Thus, in a similar manner as stated before, we find the conductance in the solid region within this time scale when the solid is decorated by the dislocation pair. This gives a heat conductance $G_s=2.29\ (\tau_s d)^{-1}$. After a further wait for $10^5\delta t$ the dislocations get annihilated. At this stage the whole trapped region is transformed into a 24-layered solid. Then the heat conductance comes out to be $G_s=3.53\ (\tau_s d)^{-1}$. Thus after complete annihilation of the dislocation pair the conductance of the solid rises by about 54%. This study already indicates towards the fact that dislocations behave like large resistances towards heat transport. One can use the presence of stable dislocation pairs as have been obtained in confined narrow strips [20,21] for a more careful study of the impact of dislocations on heat transport.

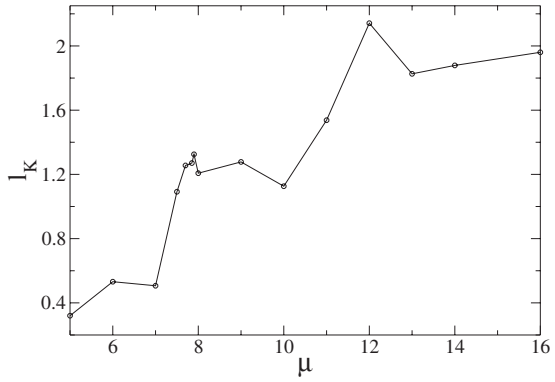

FIG. 27. Plot of Kapitza length l_K in units of L_s, as a function of μ. This shows a jump increase at the layering transition.

C. Approximate theory

We now provide an approximate theoretical approach to calculate heat conductance within the solid region. We use a free-volume-type calculation to obtain an approximate estimate for heat conductance starting from an exact expression for the αth component of the heat flux density [21]

$$j_\alpha(\mathbf{r}) = j_\alpha^K(\mathbf{r}) + j_\alpha^U(\mathbf{r}) = \sum_i \delta(\mathbf{r}-\mathbf{r}_i) h_i \mathbf{v}_i^\alpha + \frac{1}{2}\sum_{i,j\neq i} \theta(x_i^\alpha - x^\alpha) \prod_{\nu\neq\alpha} \delta(x^\nu - x_i^\nu) f_{ij}^\beta (v_i^\beta + v_j^\beta), \tag{15}$$

obtained from continuity of local energy density. Here $\theta(x)$ is the Heaviside step function and $\delta(\ldots)$ is a Dirac delta function, $h_i = m\mathbf{v}_i^2/2 + \phi(\mathbf{r}_i) + \Sigma_{i>j} u(r_{ij})$, $\phi(\mathbf{r}_i)$ is an on-site potential, and $u(r_{ij})$ is the interparticle interaction. The first term in Eq. (15), $j_\alpha^K(\mathbf{r})$ denotes convection while the second term $j_\alpha^U(\mathbf{r})$ denotes conduction. The above formula for conduction has a simple interpretation. The sum is over only those i for which $x_i^\alpha > x^\alpha$. Thus this formula gives the net rate at which work is done by particles on the left of x^α on the particles on the right, which is therefore the rate at which energy flows from left to right. The αth component of the integrated heat current density over the solid region [21] is

$$\langle I_\alpha \rangle = \sum_i \langle h_i v_i^\alpha \rangle - \frac{1}{4}\sum_{i,j\neq i} \left\langle \frac{\partial u(r_{ij})}{\partial r_{ij}} \frac{x_{ij}^\alpha x_{ij}^\beta}{r_{ij}} (v_i^\beta + v_j^\beta) \right\rangle. \tag{16}$$

In the solid region most of the transport is carried out by conduction and one may ignore the convection part. In this study we focus on the average heat current density along the y direction $j_E = \langle I_y \rangle / L_x L_s$. Ignoring convection inside the solid, approximating the system as a system of hard disks with some effective hard disk diameter σ and assuming LTE [21], the heat conductance in units of $(\tau_s d)^{-1}$ can be expressed as

$$G_s = \frac{j_E}{\Delta T} = \left[3\frac{\rho_s}{L_s}\frac{y_c^2}{\tau_c} \right] \left(\frac{d}{\sigma} \right)^2, \tag{17}$$

where $\rho_s = 4\eta_s/\pi$, y_c is the average separation between the colliding particles in the y direction, τ_c is the mean collision

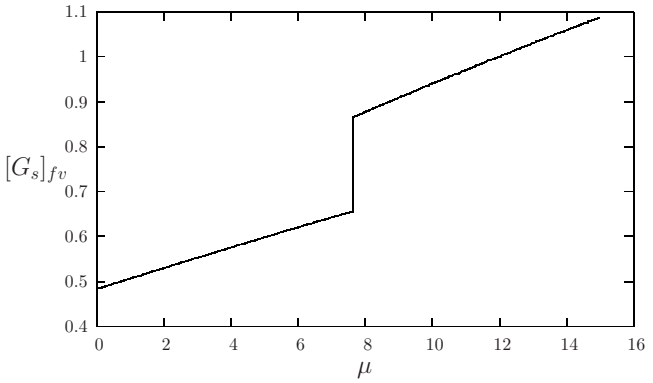

FIG. 28. Free-volume estimate of the y component of heat conductance $[G_s]_{fv}$, in units of $(\tau\sigma)^{-1}$, in the solid region of a hard disk system composed of liquid and trapped solid regions. Heat conductance shows a jump increase as a layering transition occurs with an increase in trapping potential μ.

time, and ρ_s is the average density of the solid. For the details of this derivation refer to Ref. [21]. The extra factor of $(d/\sigma)^2$ is due to the mapping of the soft disks of diameter d to the effective hard disks of diameter σ.

Now this conductance G_s can be calculated if one can obtain some estimate for y_c and τ_c. We estimate y_c^2 and τ_c from the fixed neighbor free-volume theory (FNFVT) as in Ref. [21]. For different values of (η_s, L_s) (η_s obtained by extremizing the free energy of the full system at a given potential well depth μ, as discussed in Sec. III), one can obtain $a_0, \varepsilon_{xx}, \varepsilon_{yy}$ that gives the basic geometrical inputs of b and h (Fig. 9). We assume the test particle P_0 moves in the cage formed by its neighbors and obtain the average values $[y_c^2]_{fv}$ and $[\tau_c]_{fv}$ for the moving particle from FNFVT. We assume that the position of the center of the moving disk $P_0(x,y)$, at the time of collision with the other disks, is uniformly distributed on the boundary $\mathcal{B}$ of the free volume. Then $[y_c^2]_{fv}$ can be easily calculated using the expression [21]

$$[y_c^2]_{fv} = \frac{\sum_i \int_{\mathcal{B}_i} ds(y - y_i)^2}{L_{\mathcal{B}}}, \tag{18}$$

where $\mathcal{B}_i$ is the part of the boundary $\mathcal{B}$ of the free volume when the middle disk is in contact with the ith fixed disk, ds is the infinitesimal length element on $\mathcal{B}$, while $L_{\mathcal{B}}$ is the total length of $\mathcal{B}$. An exact calculation of $[\tau_c]_{fv}$ is nontrivial. However, we expect $[\tau_c]_{fv} = c v_{fv}^{1/2}/T^{1/2}$ where v_{fv} is the "free volume" (see Fig. 9) and c is a constant factor of $O(1)$, which may be used as a fitting parameter. Thus the heat conductance in the solid region may be expressed as

$$[G_s]_{fv} = \frac{3\rho_s \sigma^2 T^{1/2}}{L_s d^2} \frac{[y_c^2]_{fv}}{c v_{fv}^{1/2}}. \tag{19}$$

There are well defined schemes [57] to approximate a soft disk system as a system of effective hard disks. However, we choose a much simpler path of finding the heat conductance of a trapped hard disk system instead. In Fig. 28 we plot $[G_s]_{fv}$ as a function of μ with $L_s = 19.73\sigma$ the same width of the trapped hard disks used in Sec. II. For hard disks we obtain heat conductance in units of $(\tau\sigma)^{-1}$ and use an average temperature $k_B T = 1$ and set $c = 1$. This gives the estimate of heat conductance along the y direction in a hard disk system that showed a layering transition from 21 to 22 layers near $\mu = 8$ in Fig. 7. The plot clearly shows the associated increase in heat conductance in the solid region. This behavior is also in qualitative agreement with Fig. 25.

With the help of these results we may conclude that the layering transition has a profound effect on the thermal properties of the trapped solid lying in contact with its liquid. An important consequence of this study is the possibility that the thermal resistance of interfaces may be altered using external potentials, which cause layering transitions in a trapped nano solid. Moreover, the heat conductance of the solid may be drastically reduced by tuning the trapping potential. We believe that these phenomena have the potential for useful applications for, e.g., as tunable thermal switches or in other nanoengineered devices.

VII. CONCLUSION

In this paper we have shown that liquid-solid interfaces, which are constrained by strong chemical potential gradients, remain flat and at the same time undergo fluctuations, which increases or decreases the number of solid layers by one. The nature of these fluctuations is strongly influenced by the size of the solid. It is expected that for macroscopically large solids these fluctuations would reduce to the random nucleation of steps on the solid surface and the sort of coherence observed here would be absent. Confining a thin "long" strip of solid by smooth walls in quasi-one-dimension leads, strictly speaking, to a destruction of solidlike order [20,35] and an enhancement of smecticlike ordering of individual layers parallel to the confining walls. It is this reduction of interlayer coupling that is ultimately responsible for the spallation of single solid layers.

Before we end, we would like to examine carefully the relevance of our results to practical situations and experimental systems constructed in a laboratory. In recent years our ability to manipulate matter at an atomic or molecular level has increased tremendously [58]. It is possible now to localize atoms using carefully designed atomic traps [30,59] and observe their properties. It is also possible to set up experiments where atoms may be picked one by one and arranged in any specified pattern [58]. Parallel to this development, one can now synthesize functionalized colloidal [27,60] particles with a variety of shapes and sizes that mimic the properties of atomic matter at length and time scales that are easy to handle even in relatively inexpensive experimental setups. Colloidal particles can also be manipulated using laser tweezers and traps [19,29,30,32], confining within narrow channels and slits [19,61], adsorbing on substrates or air-water interfaces [62], and assembling layer by layer using carefully designed substrate templates [28,63].

The structural aspects of our results, viz., the layering transition [18,19] and all associated phenomena should be observable in both atomic systems like rare gases in atom

traps and in colloids on templates or in laser fields. Indeed, interfacial fluctuations similar to the sort discussed in this paper have been observed during early nanoindentation experiments [64]. Layering transitions have also been observed in shaken hard disks more than two decades ago [65]. In confined molecular systems such layering transitions are of great relevance to the study of nanotribology [18].

The dynamical aspects of our results, on the other hand, will be difficult to observe in colloidal systems because of viscous damping by the solvent. Nevertheless, it may still be possible to observe some of these effects if this damping is small [66]. Our results for momentum and heat conduction in trapped solids therefore pertain mainly to atomic or molecular systems where such damping is absent [18]. As such, we do not see any difficulty for generalizing the main conclusions of our study to dimensions higher than two. In three dimensions, confinement to a slit should have similar effects on a three-dimensional solid, viz., reducing interlayer coupling so that two-dimensional layers may become partially independent. Weak shock waves may then be able to spallate these layers into a surrounding liquid or gaseous phase. Work along these lines is in progress.

ACKNOWLEDGMENTS

We would like to thank Madan Rao, Abhishek Dhar, Tamoghna K. Das, Kurt Binder, Andrea Ricci, and Peter Nielaba for discussions and Martin Zapotocky for a critical reading of the manuscript. This work was partially supported by the Department of Science and Technology and CSIR (India).

[1] B. Widom, in *Phase Transitions and Critical Phenomena*, edited by C. Domb and M. S. Green (Academic, New York, 1972), Vol. 2.
[2] J. D. van der Waals, Verh.-K. Ned. Akad. Wet., Afd. Natuurkd., Eerste Reeks **1**, 8 (1893).
[3] J. W. Cahn and J. E. Hilliard, J. Chem. Phys. **28**, 258 (1958).
[4] S. A. Safran, *Statistical Thermodynamics of Surfaces. Interfaces and Membranes* (Addison Wesley, Reading, MA, 1994).
[5] J. S. Rowlinson and B. Widom, *Molecular Theory of Capillarity* (Clarendon, Oxford, 1982).
[6] K. Binder and M. Müller, Int. J. Mod. Phys. C **11**, 1093 (2000).
[7] A. L. Barabasi and H. E. Stanley, *Fractal Concepts in Crystal Growth* (Cambridge University Press, Cambridge, England, 1995).
[8] S. F. Edwards and D. R. Wilkinson, Proc. R. Soc. London, Ser. A **381**, 17 (1982).
[9] A. Werner F. Schmid, M. Müller, and K. Binder, J. Chem. Phys. **107**, 8175 (1997).
[10] K. Binder, D. P. Landau, and A. M. Ferrenberg, Phys. Rev. Lett. **74**, 298 (1995); Phys. Rev. E **51**, 2823 (1995).
[11] T. Kerle, J. Klein, and K. Binder, Phys. Rev. Lett. **77**, 1318 (1996); Eur. Phys. J. B **7**, 401 (1999).
[12] B. J. Schulz, B. Dunweg, K. Binder, and M. Muller, Phys. Rev. Lett. **95**, 096101 (2005).
[13] S. Balibar, H. Alles, and A. Y. Parshin, Rev. Mod. Phys. **77**, 317 (2005).
[14] A. Chaudhuri, P. A. Sreeram, and S. Sengupta, Phase Transitions **77**, 691 (2004); Phys. Rev. Lett. **89**, 176101 (2002).
[15] A. Chaudhuri, S. Sengupta, and M. Rao, Phys. Rev. Lett. **95**, 266103 (2005).
[16] D. Chaudhuri, A. Chaudhuri, and S. Sengupta, J. Phys.: Condens. Matter **19**, 152201 (2007).
[17] D. Frenkel and B. Smit, *Understanding Molecular Simulations* (North Holland, Amsterdam, 2000).
[18] C. Ghatak and K. G. Ayappa, Phys. Rev. E **64**, 051507 (2001); K. G. Ayappa and C. Ghatak, J. Chem. Phys. **117**, 5373 (2002).
[19] M. Schmidt and H. Löwen, Phys. Rev. E **55**, 7228 (1997); A. Fortini and M. Dijkstra, J. Phys.: Condens. Matter **18**, L371 (2006); A. H. Marcus and S. A. Rice, Phys. Rev. E **55**, 637 (1996); R. Zangi and S. A. Rice, *ibid.* **61**, 660 (2000).
[20] D. Chaudhuri and S. Sengupta, Phys. Rev. Lett. **93**, 115702 (2004).
[21] D. Chaudhuri and A. Dhar, Phys. Rev. E **74**, 016114 (2006).
[22] Robert W. Cahn and Peter Haasen, *Physical Metallurgy* (North-Holland, Amsterdam, 1996).
[23] J. Fineberg and M. Marder, Phys. Rep. **313**, 1 (1999).
[24] Y. B. Zeldovich and Y. P. Raizer, *Physics of Shock Waves and High-Temperature Hydrodynamic Phenomena* (Dover Publications, New York, 2002).
[25] J.-L. Barrat and F. Chiaruttini, Mol. Phys. **101**, 1605 (2003).
[26] P. L. Kapitza, Zh. Eksp. Teor. Fiz. **11**, 1 (1941) [J. Phys. (USSR) **4**, 181 (1941)]; *Collected Papers of P. L. Kapitza*, edited by D. ter Haar (Pergamon Press Ltd., Oxford, England, 1967), Vol. II; G. L. Pollack, Rev. Mod. Phys. **41**, 48 (1969).
[27] I. W. Hamley, *Introduction to Soft Matter: Polymer, Colloids, Amphiphiles and Liquid Crystals* (Wiley, Cluchester, 2000).
[28] J. P. Hoogenboom D. L. J. Vossen, C. Faivre-Moskalenko, M. Dogterom, and A. van Blaaderen, Appl. Phys. Lett. **80**, 4828 (2002).
[29] J. Baumgartl, M. Brunner, and C. Bechinger, Phys. Rev. Lett. **93**, 168301 (2004).
[30] W. D. Phillips, Rev. Mod. Phys. **70**, 721 (1998).
[31] H. J. Metcalf and P. van der Straten, *Laser Cooling and Trapping* (Springer, Heidelberg, 1999).
[32] David G. Grier, Nature (London) **424**, 810 (2003).
[33] A. Jaster, Physica A **277**, 106 (2000).
[34] P. M. Chaikin and T. C. Lubensky, *Principles of Condensed Matter Physics* (Cambridge University Press, Cambridge, 1995).
[35] A. Ricci, P. Nielaba, S. Sengupta, and K. Binder, Phys. Rev. E **74**, 010404(R) (2006); Phys. Rev. E **75**, 011405 (
[36] P. G. deGennes, *ibid.* **6**, 1448 (1990).
[37] L. D. Landau and E. M. Lifshitz, *Theory of Elasticity*, 2nd ed. (Pergamon Press, Oxford, 1987).
[38] A. Santos, M. L. de Haro, and S. B. Yuste, J. Chem. Phys. **103**, 4622 (1995).

[39] D. Chauhduri and S. Sengupta, e-print arXiv:0705.3135 (unpublished).
[40] J. Q. Broughton, G. H. Gilmer, and J. D. Weeks, Phys. Rev. B **25**, 4651 (1982).
[41] S. Toxvaerd, Phys. Rev. A **24**, 2735 (1981).
[42] L. D. Landau and E. M. Lifshitz, *Fluid Mechanics*, 2nd ed. (Pergamon Press, Oxford, 1987).
[43] C. Zener, Phys. Rev. **53**, 90 (1938).
[44] M. A. Isakovich, Zh. Eksp. Teor. Fiz. **18**, 907 (1948).
[45] A. Onuki, Phys. Rev. A **43**, 6740 (1991).
[46] S. Psakhie, Bull. Am. Phys. Soc. **46**, C3.005 (2001).
[47] K. S. Novoselov *et al.*, Proc. Natl. Acad. Sci. U.S.A. **102**, 10451 (2005).
[48] D. G. Cahill *et al.*, J. Appl. Phys. **93**, 793 (2003).
[49] S. Chapman and T. G. Cowling, *The Mathematical Theory of Non-uniform Gases*, 3rd ed. (Cambridge University Press, London, 1970).
[50] J. J. Erpenbeck and W. W. Wood, Phys. Rev. A **26**, 1648 (1982).
[51] W. G. Hoover, D. J. Evans, R. B. Hickman, A. J. C. Ladd, W. T. Ashurst, and B. Moran, Phys. Rev. A **22**, 1690 (1980).
[52] S. Lepri, R. Livi, and A. Politi, Phys. Rep. **377**, 1 (2003).
[53] F. Bonetto, J. Lebowitz, and L. Rey-Bellet, in *Mathematical Physics 2000*, edited by, A. F. *et al.* (Imperial College Press, London, 2000), p. 128.
[54] P. Grassberger and L. Yang, e-print arXiv:cond-mat/0204247.
[55] S. Datta, D. Chaudhuri, T. Saha-Dasgupta, and S. Sengupta, Europhys. Lett. **73**, 765 (2006).
[56] Stefan Luding, Phys. Rev. E **63**, 042201 (2001).
[57] J. P. Hansen and I. R. MacDonald, *Theory of Simple Liquids* (Wiley, Cluchester, 1989).
[58] C. P. Poole and F. J. Owens, *Introduction to Nanotechnology* (Wiley, Hoboken, NJ, 2003); V. Balzani, M. Venturi, and A. Credi, *Molecular Devices and Machines: A Journey into the Nano World* (Wiley-VCH, Weinheim, 2003).
[59] H. J. Metcalf and P. van der Straten, *Laser Cooling and Trapping* (Springer, Heidelberg, 1999).
[60] A. van Blaaderen, Nature (London) **439**, 545 (2006); A. Yethiraj and A. van Blaaderen, *ibid.* **421**, 513 (2003); A. Yethiraj, A. Wouterse, B. Groh, and A. van Blaaderen, Phys. Rev. Lett. **92**, 058301 (2004).
[61] R. Haghgooie and P. S. Doyle, Phys. Rev. E **70**, 061408 (2004); Phys. Rev. E **72**, 011405 (2005).
[62] K. Zahn, J. M. Mendez-Alcaraz, and G. Maret, Phys. Rev. Lett. **79**, 175 (1997); K. Zahn, R. Lenke, and G. Maret, *ibid.* **82**, 2721 (1999); K. Zahn and G. Maret, *ibid.* **85**, 3656 (2000).
[63] Jacob Hoogenboom, Colloidal Epitaxy: A Real-Space Analysis, Ph.D. thesis, University of Utrecht, 2002 (unpublished).
[64] U. Landman *et al.*, Science **248**, 454 (1990); A. P. Sutton and J. B. Pethica, J. Phys.: Condens. Matter **2**, 5317 (1990).
[65] P. Pieranski J. Malecki, and K. Wojciechowski, Mol. Phys. **40**, 225 (1980).
[66] S. Ramaswamy and G. F. Mazenko, Phys. Rev. A **26**, 1735 (1982).